8-2017

Multi-stability and Variable Stiffness of Cellular Solids Based on Origami Patterns

Sattam Sengupta
Clemson University, ssengup@clemson.edu

MULTI-STABILITY AND VARIABLE STIFFNESS OF CELLULAR SOLIDS BASED ON ORIGAMI PATTERNS

A Thesis
Presented to
the Graduate School of
Clemson University

In Partial Fulfillment
of the Requirements for the Degree
Master of Science
Mechanical Engineering

---

by
Sattam Sengupta
August 2017

Accepted by:
Dr. Suyi Li, Committee Chair
Dr. Joshua Summers
Dr. Oliver Myers

ABSTRACT

The application of origami patterns in engineering design has been the subject of much research efforts. Structures derived based on origami patterns are capable of displaying a host of innovative mechanical properties which are directly related to the kinematics of their folding. The work presented in this research takes design inspiration from a rigid foldable type of origami, namely the Miura-ori pattern. A cellular solid designed based on the Miura Ori folding pattern can exhibit three dimensional multi-stability, and different programmable characteristics like variable stiffness and elastic moduli, which stem from the inherent elastic multi-stability. The Miura Ori structure can be broken down to a basic building block termed as a unit Miura cell. This unit cell inherits its bistability from the nonlinear relationship between the external deformation and the folding of the cell. Unlike other conventional bistable mechanisms such as curved beams or asymmetric laminar composites, this unit cell possess an unorthodox characteristic; the critical, unstable equilibrium configuration lies on the same side of the two stable ones. This leads to two distinct force deformation curves within the same range and thereby leading to two distinct stiffness magnitudes at the two stable configurations. The difference in the stiffness magnitudes between the two stable configurations can be tweaked by tailoring certain key design parameters of the unit cell. The programmable properties of the bistable unit cell can be further extended to include variable effective elastic modulus since it can be directly related to the stiffness. This research focuses on the comprehensive study and design of such a bistable unit Miura cell with programmable mechanical properties. The results from the study of this cell are qualitatively validated using a 3D

printed prototype. The analysis of the unit cell also paves the way for extending the study where identical unit cells are assembled to form a multi-stable Miura structure with programmable stiffness and effective elastic modulus.

DEDICATION

I dedicate this thesis to my parents.

ACKNOWLEDGMENTS

I would like to thank my advisory committee chair, Dr. Suyi Li, for providing me with the opportunity to work on this research and guiding me throughout. His expertise and mentorship have helped me to be a better researcher, and also improve my professional skills. I thank him again for always supporting me and guiding me in the right direction. I would also like to thank Dr. Joshua Summers and Dr. Oliver Myers for serving on my thesis advisory committee.

I would like to thank my fellow lab-mates at 256 EIB for their help and feedback over the course of this work. I would also like to thank the Mechanical Engineering department here at Clemson for providing financial assistance for my graduate studies.

Finally, I thank my mum and dad for their unwavering belief in me. This would not have been possible without them. Also, thanks to a lot of my friends who helped me make the decision to attend grad school and supported me throughout.

TABLE OF CONTENTS

Page

Table of Contents (Continued) Page

LIST OF TABLES

LIST OF FIGURES

List of Figures (Continued)

Figure Page

List of Figures (Continued)

CHAPTER ONE

INTRODUCTION

Origami is an ancient Japanese art form which was initially used to fold paper in order to create intricate, artistic and decorative patterns. This art was developed in the early 1600s [1] and has been traditionally used for artistic portrayals. Origami involves folding of paper into basic folds like mountain and valley folds, pleats or reverse folds.

Over the last five decades, emerging mathematical theories pertaining to paper folding have led to an increase in the number of engineering applications based on origami designs. In particular, it is possible to have various new applications based on origami concepts in the field of mechanical engineering. In this introductory chapter one, the research objective, current state of the art of origami-inspired engineering applications, and the outline of the thesis are provided.

1.1 Origami in Engineering

There are a wide array of disciplines under origami which can be exploited for mechanical engineering applications. Greenberg et al. [2] identified “orimimetics” as the ability to use the concept of folding and apply it to solve engineering problems. Their work proposed the feasibility of designing compliant mechanisms based on the flat folding paper mechanisms derived from origami patterns. Action origami is another type of origami design where the patterns exhibit motion in their final folded state. Bowen et al. [3, 4] identified various types of action origami which can have potential application in engineering designs. Kirigami is another variation of origami where, in addition to folding,

cutting in the paper is also incorporated. A host of active research areas of applying kirigami concepts to engineering include nanocomposites for various electronic and optoelectronic devices and other applications involving morphing structures. Another specific application of kirigami is the design of a morphing cellular wingbox to achieve variable operational configurations for an aircraft in cruise [5, 6, and 7]. Lastly, an important type of origami which can be identified to have engineering applications is rigid-foldable origami. In this type of origami, the creases can be assumed to act as hinges and the flat surfaces are assumed to be completely rigid so that there is no bending deformation, only folding at the creases. The feasibility of applying the folding mechanisms of origami to engineered structures was extensively reviewed by Lebée in [8]. Peraza-Hernandez et al. also reviewed the various potential applications of using origami inspired patterns to design active-structures capable of self-folding [9]. The work presented here is based on the Miura-Ori origami pattern, which is a kind of rigid foldable origami.

The applications of Miura folding patterns in engineering is by no means a recent effort. The earliest documented engineering applications include using Miura fold pattern in solar panels used in spacecrafts, deployable space cranes and other large membranes in space [10, 11, and 12]. These Miura patterns help to stow all the space paraphernalia onboard spacecraft in a very compact manner which could then be manually or autonomously deployed once in space. Recent research suggests that Miura-Ori sheets can be used to form structures which can be capable of shape morphology [13]. A comprehensive review of these applications of Miura-Ori and other origami patterns in engineering including different types of structures, packaging and storage devices and

mechanisms used for manufacturing is provided by Turner et al. in [16]. Since the Miura Ori design is a type of a rigid foldable pattern, the facets are assumed to be perfectly rigid and the creases behave similar to hinges. Because of this rigid foldability, a single force can be used to fold or unfold the entire structure.

This work will focus on a particularly interesting concept of stacked Miura-Ori. When multiple Miura Ori sheets are stacked, a three dimensional cellular solid is formed (Figure 1.1 a, b), whose characteristics are dictated by the kinematics of folding. There are certain design constraints for the proper stacking of the two Miura sheets which will be explained in detail in a subsequent chapter. The nonlinear correlations between the folding of the Miura sheets and the external deformations of the structure can be harnessed to achieve many unique mechanical properties. For example, Schenk and Guest [14] described how a metamaterial using Miura fold patterns can display both positive and negative Poisson's ratio based on different modes of deformation. 4-vertex Miura sheets can show self-locking because of facet-binding and this can be used to develop a system with vibration isolation or discrete stiffness jumps [15]. Another area where a lot of current research is presently focused is on the elastic multi-stability achieved in Miura solids [17, 18, 19, 20, and 21]. For the stacked origami, multi-stability means that the overall Miura solid can possess multiple stable states based on the folding configurations. An external force can be used to switch the solid from one stable configuration to another without the necessity of a continuous force to hold it in a specific configuration (figure 1.1 c).

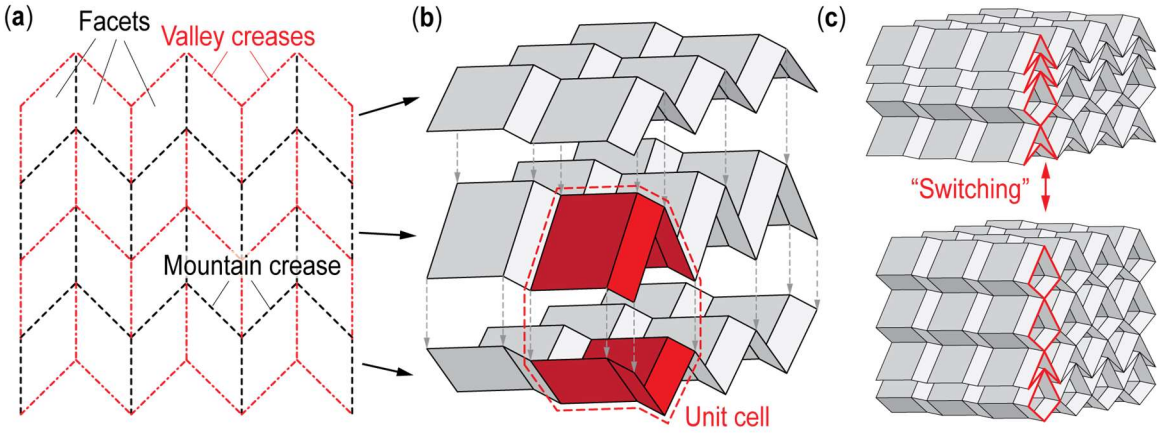

Figure 1.1 A layout of a Miura pattern with valley and mountain folds (a), stacking Miura sheets to form a unit cell (b) and switching between different configurations in a multi-stable Miura solid (c).

Multi-stability is particularly interesting because it can lead to new programmable functionalities. For example, shape morphing, vibration isolation, energy harvesting, and impact absorption have been achieved on a variety of bistable structures such as curved beam and asymmetric composite laminates. However, these existing multi-stable mechanisms are capable of displaying only one-dimensional multi-stability i.e. the beams are only bistable in the direction perpendicular to the beam surface thereby limiting their potential. The multi-stability in Miura structures, on the other hand, are fundamentally three-dimensional since these structures are capable of shape transformation along their height, length and width. Due to this unique three-dimensional multi-stability, adaptive mechanical properties such as variable stiffness and variable elastic modulus can be harnessed in these Miura structures.

1.2 Research Objective

Therefore, the objective of this research is to examine how the three dimensional multi-stability of the stacked Miura-ori can be harnessed to achieve variable stiffness. This three dimensional Miura solid is composed of multiple unit cells. Assuming that all of these unit cells are identical, this research studies the characteristics of a single unit cell which can be seen as building block for the entire solid. The study will also aim to highlight how this variable stiffness can be programmed by tailoring the basic geometric parameters of the unit cell within a chosen design space. Since the effective elastic modulus of the unit cell can be formulated from its stiffness, the study is also extended to show the unit cell can achieve variable elastic modulus. From the design space mapped out in the study, a CAD model is generated and a prototype is 3D printed. This prototype is tested to show bistability and the variable stiffness in order to validate the study. Additionally, the results of the study for the unit cell can be applied to a Miura chain and certain hypotheses can be made regarding the mechanical properties of this solid.

1.3 Outline of the Thesis

This section provides a summary of the chapter presented in this thesis here forth.

Chapter Two explains how a unit cell is defined when two Miura sheets are stacked according to the specific design constraints, and defines the parameters of the unit cell.

Chapter Three discusses the mechanics behind the bistable nature of the unit cell and discusses how the stiffness magnitudes are derived for the two stable configurations.

Chapter Four highlights the results from an exhaustive parametric study of the unit Miura cell and identifies key parameters and the design space for the bistability of the cell.

Chapter Five provides the experimental results from the testing of a 3D-printed unit cell prototype and compares the experimental results against the theoretical ones.

Chapter Six extends the study of the unit cell to a Miura chain and summarizes certain insights from the analysis of this chain.

Chapter Seven sums up the conclusions and identifies key areas where further research can be directed to extend this study.

A pictorial outline of this thesis is illustrated in Figure 1.2.

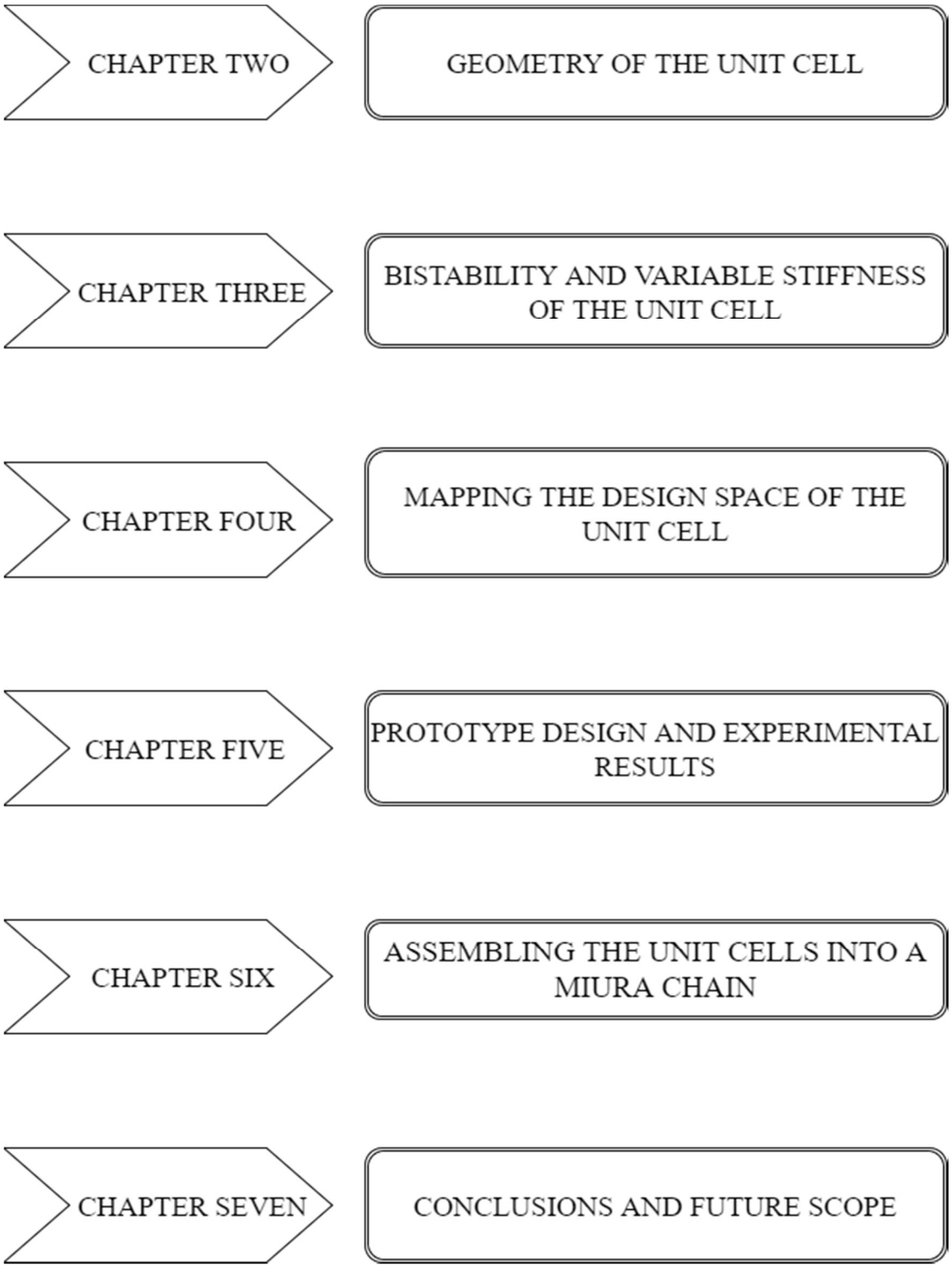

Figure 1.2 Pictorial outline of the thesis

CHAPTER TWO

GEOMETRY OF THE UNIT CELL

When two compatible Miura Ori sheets are stacked on top of each other along their crease lines, a unit Miura cell is formed. The entire Miura Ori solid is a periodic tessellation formed from such identical unit cells. Because of this, the geometry of a unit cell is studied in this section in depth and the results and conclusions from the study of this unit cell can be applied to the entire Miura structure. This chapter discusses the design constraints that need to be met for two Miura sheets to be kinematically compatible so that a unit cell can be formed and then highlights the important parameters which define the shape and folding motion of the unit cell.

2.1 Design of Miura sheets to form a unit cell

The cardinal parts of a Miura pattern are its facets, which are assumed to be rigid, and the creases between the facets which act as torsional hinges with a certain amount of stiffness. The basic geometric parameters which define a Miura facet are the lengths of its two sides (a_k and b_k), and the sector angle between these adjacent facets (γ_k) as shown in Figure 2.1. The subscript 'k (= I or II)' stands for the two different Miura sheets which make up the unit cell. This work presented here assumes that the Miura with the shorter crease length is denoted by 'I'. These three basic geometric parameters remain constant over the entire folding range of the unit cell. In order to describe the folding motion of the cell, a dihedral angle (θ_k) is defined between the Miura facets and the x-y reference plane. These parameters are illustrated in Figure 2.1. Previous research [11] has identified three

design constraints the two Miura sheets have to satisfy so that they are compatible and always remain connected:

$$b_{II} = b_I \tag{1}$$

$$\frac{\cos\gamma_{II}}{\cos\gamma_I} = \frac{a_I}{a_{II}} \tag{2}$$

$$\frac{\cos\theta_{\mathrm{II}}}{\cos\theta_{\mathrm{I}}} = \frac{\tan\gamma_{\mathrm{I}}}{\tan\gamma_{\mathrm{II}}}. \tag{3}$$

2.2 Specifications of a unit Miura cell

The complete folding range of the Miura sheets are defined by varying θ_I from $-(\pi/2)$ to $(\pi/2)$. It is important to note that for one θ_{II}, there exist two corresponding θ_I angles of the same magnitude but opposite signs. Since θ_I and θ_{II} are constrained from equation (3), i.e. θ_{II} changes with any change in θ_I, the folding mechanism of the unit cell still has only one degree of freedom. In this work, θ_I is chosen as the independent dihedral angle which defines the folding motion of the unit cell and further, for the sake of brevity, is denoted as simply θ. The folding angles of the cell at the two stable configurations are dented by $\theta_k°$ and are termed as the stress free folding angles. The external dimensions of the unit cell along the x, y and z planes change over the folding range of the cell and can be defined as a function of the folding angle θ [21].

$$L = 2b_{\mathrm{I}}\cos\theta\tan\gamma_{\mathrm{I}}\left(1+\cos^2\theta\tan^2\gamma_{\mathrm{I}}\right)^{-1} \tag{4}$$

$$W = 2a_{\mathrm{I}}\sqrt{1-\sin^2\theta\sin^2\gamma_{\mathrm{I}}} \tag{5}$$

$$H = a_{\mathrm{I}} \sin\gamma_{\mathrm{I}} \left(\sqrt{\frac{\tan^2 \gamma_{\mathrm{II}}}{\tan^2 \gamma_{\mathrm{I}}} - \cos^2 \theta} - \sin\theta \right) \tag{6}$$

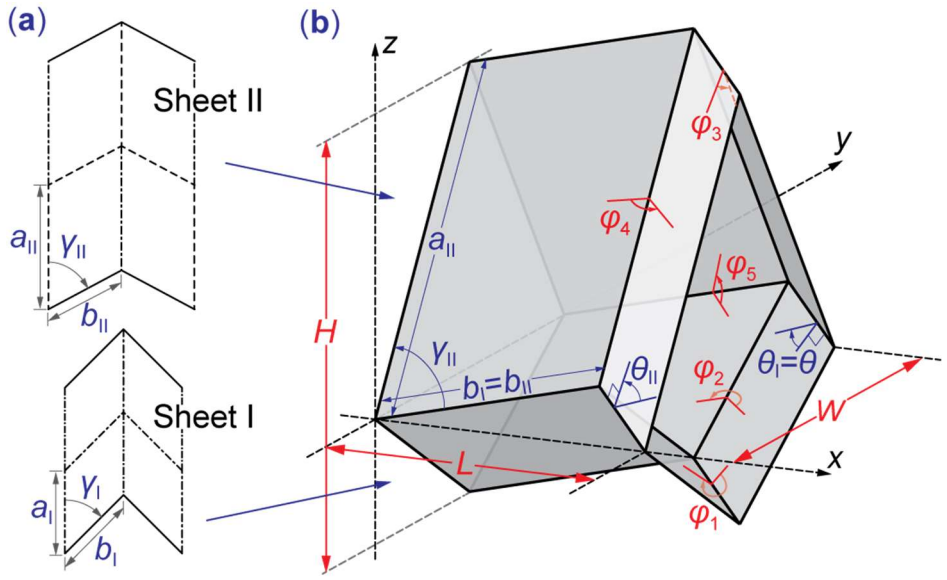

Figure 2.1 Two kinematically compatible Miura sheets (a) and the unit cell formed by stacking these Miura sheets along with all design parameters (b)

In Figure 2.2, the dimensions of the unit cell along the *x, y* and *z* planes i.e. the length, width and height are plotted over the entire range of the folding motion of the unit cell. It can be seen that the height of the cell continuously decreases as the cell folds or in other words, the relation between the height and the folding angle is strictly monotonic. However, both the length and width of the unit cell initially increase and then decrease over the folding range. Both the length and width reach their maximum values at $\theta = 0$. The folding angles of the cell at the two stable configurations are dented by $\theta_k°$ and are termed as the stress free folding angles. This nonlinear relation is the root cause of an

unconventional bistable nature of the unit cell along its length and width, which will be discussed soon in the next chapter.

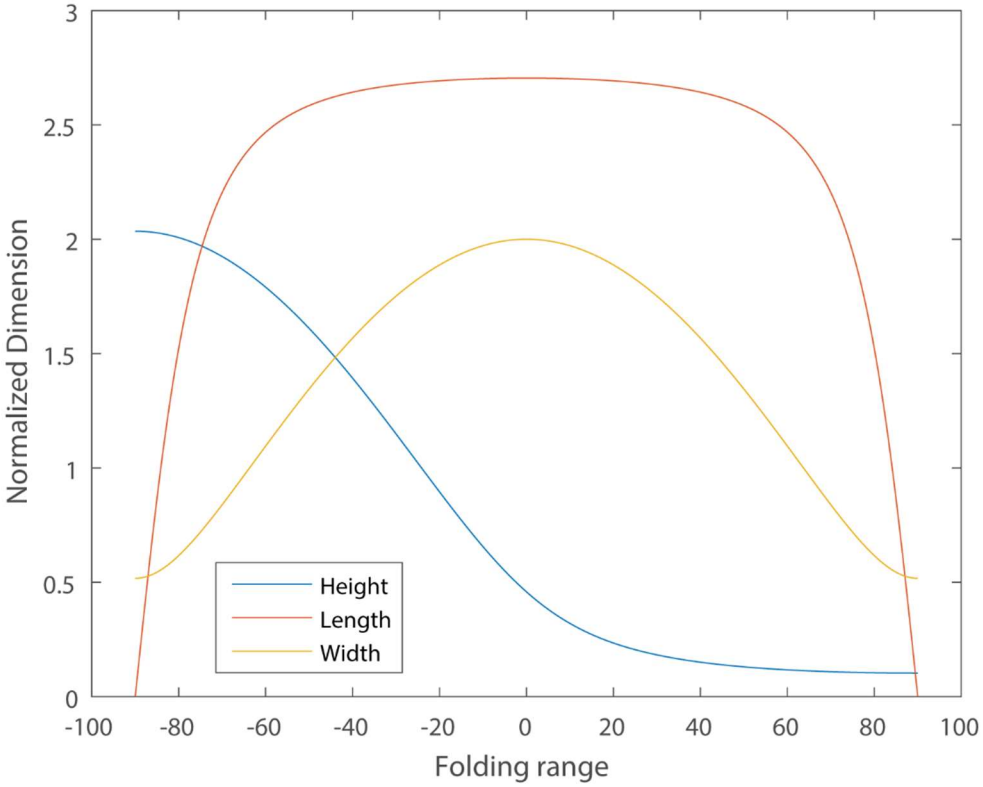

Figure 2.2 Relation between the cell dimensions and the folding angle

There are five dihedral angles between adjacent facets of the unit cell shown in Figure 2.1 which vary with the folding of the unit cell. The values of these dihedral angles are also illustrated in Figure 2.3 along the folding angle θ.

$$\varphi_1 = \pi - 2\theta \tag{7}$$

$$\varphi_2 = 2\sin^{-1}\left(\frac{\cos\theta}{\sqrt{1-\sin^2\theta\sin^2\gamma_I}}\right) \tag{8}$$

$$\varphi_3 = \pi - 2\cos^{-1}\left(\tan\gamma_{II}\tan^{-1}\gamma_I\cos\theta\right) \tag{9}$$

$$\varphi_4 = 2\sin^{-1}\left(\frac{\sin\gamma_I}{\sin\gamma_{II}}\sin\frac{\varphi_2}{2}\right) \tag{10}$$

$$\varphi_5 = \cos^{-1}\left(\tan\gamma_{II}\tan^{-1}\gamma_I\cos\theta\right) - \theta \tag{11}$$

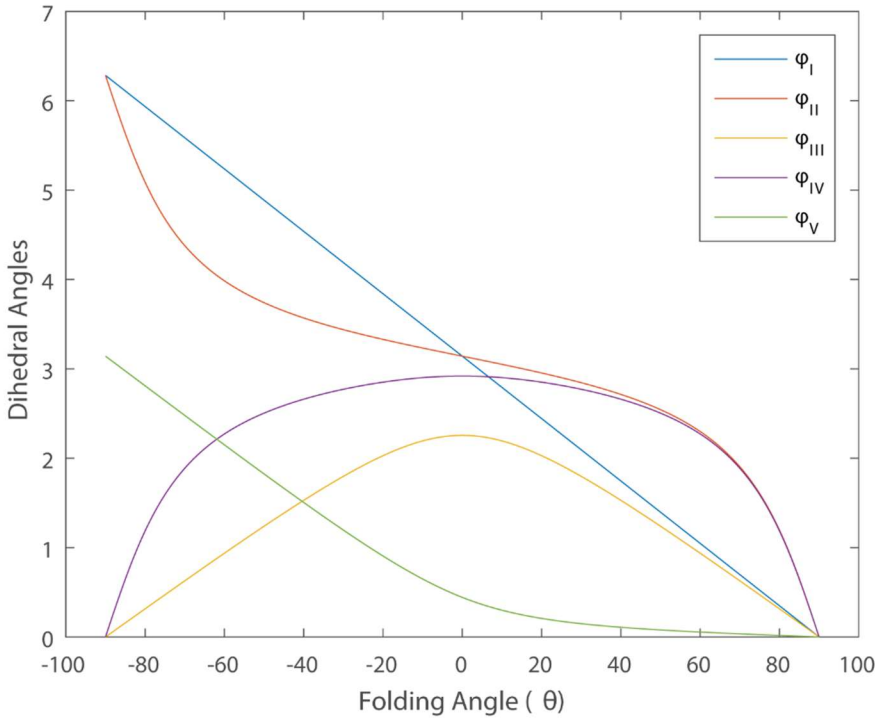

Figure 2.3 Dihedral angles of the unit cell over the folding angle

All of these parameters and the relations between have been adapted from previous work [14 and 21] and they define the unit cell. The next chapter continues with the explanation of the unit cell in further detail by describing the parameters and terms which define the creases and how they relate to the bistable nature of the cell.

CHAPTER THREE

BISTABILITY AND VARIABLE STIFFNESS OF THE UNIT CELL

In the previous chapters, the nonlinear relationship between the external deformation and the folding of the unit Miura cell was established. This chapter expands on this relationship further and subsequently goes on to explain how the bistable nature of the unit cell is unorthodox thereby making it possible to achieve the desired variable stiffness and variable elastic modulus.

The Miura pattern being a rigid foldable pattern, the facets are assumed to be rigid, so the folding motion of the unit cell is characterized primarily by the crease folding. Since these creases act as hinges, it is assumed that they possess a certain magnitude of torsional spring stiffness *per unit length* (k_k). There are three distinct crease spring stiffnesses, k_I and k_{II} for the two Miura sheets and k_c for the crease which connects the two Miura sheets. From these, five torsional spring stiffness constants can be defined corresponding to the five dihedral angles between the facets of the unit cell. The numerical constants in the following equations are the number of creases that have the same dihedral angle.

$$K_1 = 2k_{\mathrm{I}}b \tag{12}$$

$$K_2 = 2k_{\mathrm{I}}a_{\mathrm{I}} \tag{13}$$

$$K_3 = 2k_{\mathrm{II}}b \tag{14}$$

$$K_4 = 2k_{\mathrm{II}}a_{\mathrm{II}} \tag{15}$$

$$K_5 = 4k_c b \tag{16}$$

Before starting with the explanation of the nature of bistability and the subsequent variable stiffness of the unit cell, a set of design parameters which are chosen as a case study shown in Table 3.1. These design parameters are used in all of the calculations and graphs represented here forth unless mentioned otherwise.

	Design Parameter	**Value**
Geometric Parameters (Figure 2.1a)	Crease length a_I	25 mm
	Crease length a_{II}	27.5 mm
	Crease length b	35 mm
	Sector angle γ_I	75°
	Stress free folding angle θ°	-60°
Material Parameters, aka. Crease stiffness per unit length.	k_I	5 N
	k_{II}	50 N
	k_c	5 N

Table 3.1 Input parameters used in the design study

3.1 Elastic Potential Energy of the cell

The elastic potential energy of the unit cell is a summation of the all the torsional spring energy from the creases. Since the torsional spring constants were calculated for each of the five dihedral angles (equations 12 - 16), the total elastic potential energy of the unit cell is:

$$E = \frac{1}{2}\sum_{i=1}^{5} K_i \left(\varphi_i - \varphi_i^{\circ}\right)^2 \tag{17}$$

where φ_i° are the dihedral angles corresponding to a stress-free folding angle ($\theta°$), where no creases are subjected to any folding deformation. This elastic energy can be used to plot the energy landscape of the unit Miura cell over its entire folding range shown below in Figure 3.1.

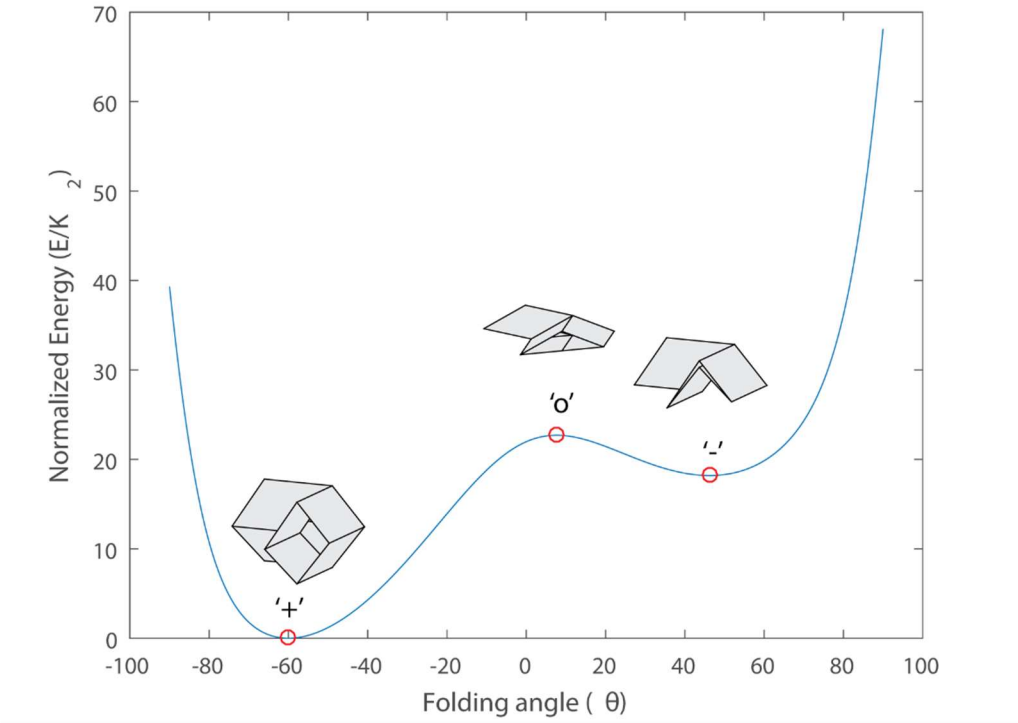

Figure 3.1 Energy landscape of the unit cell

Over the range of folding of the unit cell, there exist three equilibrium conditions which can be used to define the bistability of the cell. Of these, two configurations are the stable ones, denoted as the '+' configuration ($\theta < 0$) where the cell bulges out and the '-' configuration where the cell nests in ($\theta > 0$) as shown in Figure 3.1. The third configuration is the critical unstable equilibrium condition denoted by 'o' ($\theta = 0$). The two stable configurations, '+' and '-' can be seen represented as the two wells on the energy

landscape. This double-well energy pattern is the defining characteristics of bistable systems or mechanisms. The folding angle is -60° for the '+' configuration as stated in Table 3.1, and 7° and 46° for the 'o' and '-' configurations respectively. It is easier to design an effective bistable cell when the stress free folding angle is significantly different from 0°. This ensures that the two stable configurations maintain enough separation when they cross over the critical unstable equilibrium condition when they snap to the other stable configuration.

3.2 Variable Stiffness of the cell

The energy landscape of the unit cell in figure 3.1 is plotted with respect to folding angle θ. Such a plot is helpful for effectively illustrating the bistable nature of the unit cell, but it is necessary to study the potential energy change with respect to the external deformation of the cell in order to calculate the stiffness. The first order derivative of the energy from equation 17 will result in the force deformation curves along the height, length and width of the cell.

$$F = \frac{\partial E}{\partial X} = \frac{\partial E}{\partial \theta}\left(\frac{\partial X}{\partial \theta}\right)^{-1} \tag{18}$$

where, X can be the height, length or width. Looking at the energy of the cell along its height (Figure 3.2), it can be seen that the two stable configurations ('+' and '-') lie on the opposite sides of the critical unstable configuration ('o'). This is because of the monotonic relationship between height and the folding angle of the cell as described earlier (figure 2.2). This characteristic is common to other conventional previously mentioned

bistable mechanisms as curved beams and composite laminates. The first order derivative of the energy curve gives the force deformation curve along the height which is also shown in Figure 3.2. It can be noted that the '+','o' and '-' configurations are at located at the points where the force curve crosses over zero.

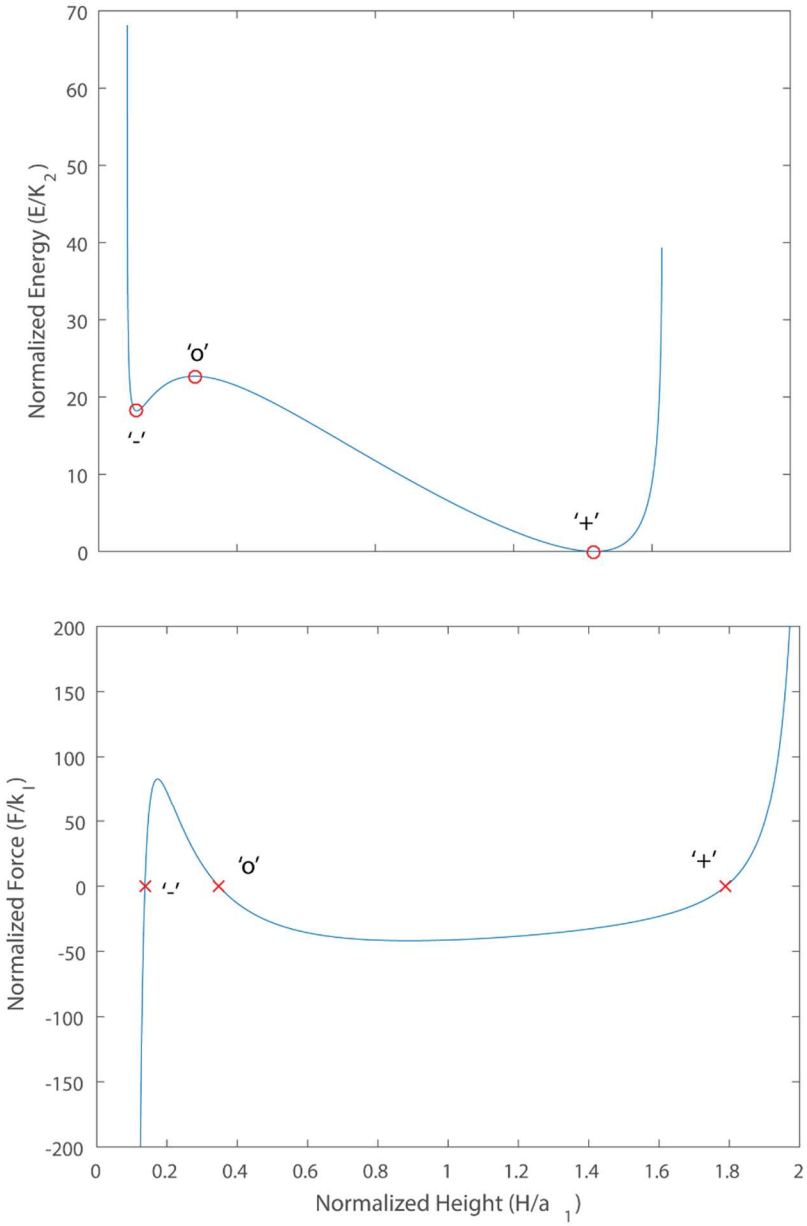

Figure 3.2 Energy and Force along the height of the cell

Unlike the behavior along the height of cell, when the energy is plotted against the length and width, it can be seen that the two stable configurations lie on the same side as the unstable equilibrium configuration. This is because of the nonlinear relationship between the length or the width and the folding angle as seen earlier in Figure 2.2.

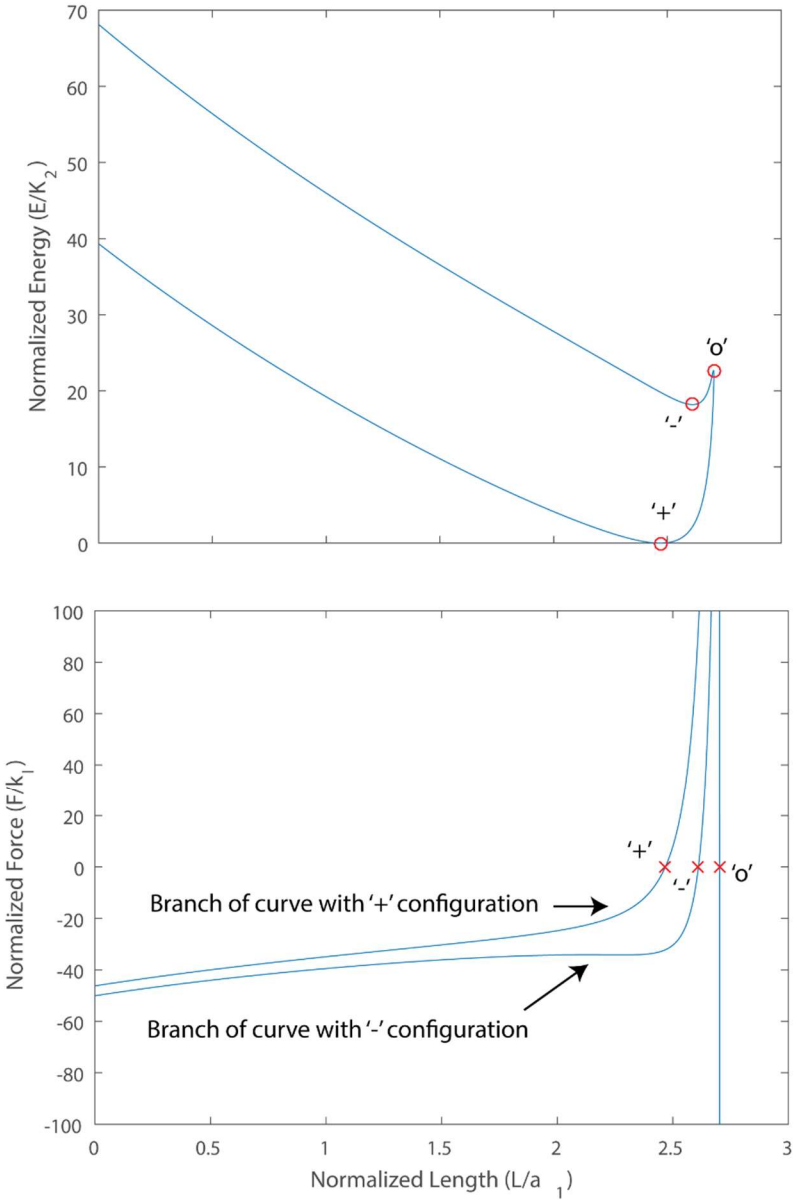

Figure 3.3 Energy and Force along the length of the cell

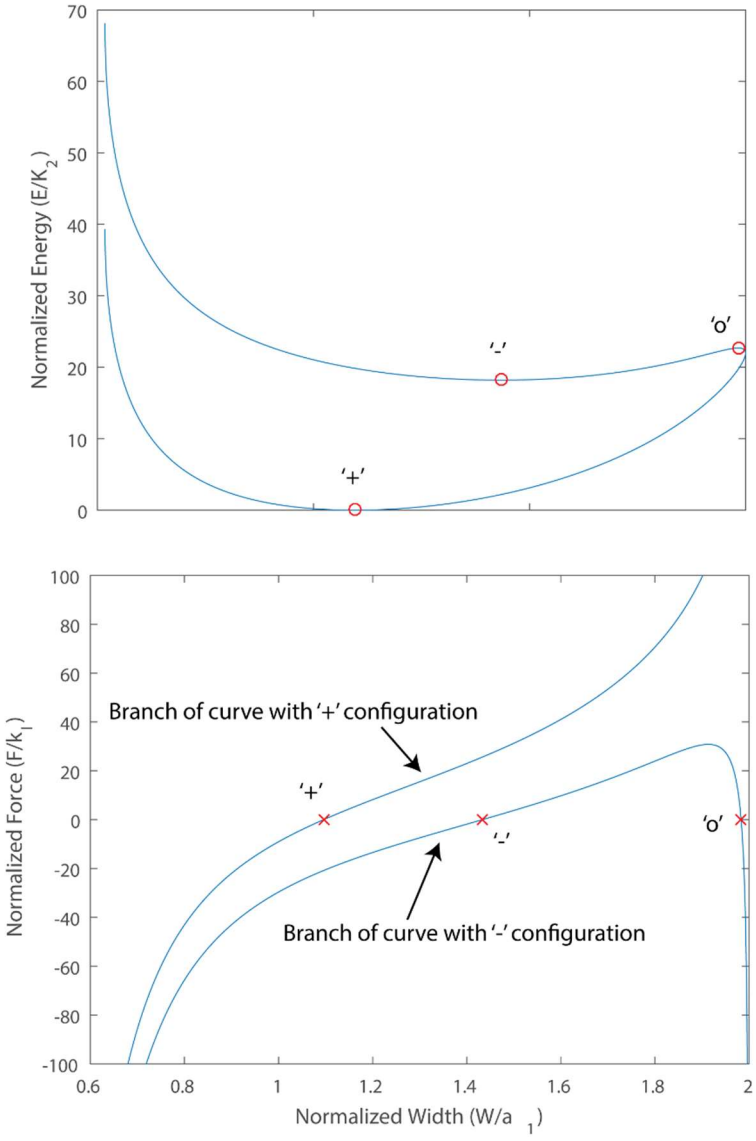

Figure 3.4 Energy and Force along the width of the cell

Another aspect of this unconventional distribution is that the unstable equilibrium can be very close to the maximum length or width allowed over the complete folding range of the unit cell. This leads to the unit cell *appearing* mono-stable over a large range of its deformation. The cell can only switch to another stable configuration when it is almost

stretched to a maximum where it reaches the critical equilibrium snap-through point. This unorthodox behavior is used to harness variable stiffness in the unit Miura cell.

From the force deformations curves shown in Figures 3.3 and 3.4, it can be seen that there exist two distinct branches of the curve along both the length and width directions. Both these branches exist within the same range of deformation of the cell. It is also seen that the slope of both the branches of the curve increase significantly close to the maximum length or width. This is because once the unit Miura cell is stretched to its maximum dimensions, the external forces directly act on the facets which are assumed to be rigid. However, such rigid facet assumption will not defeat the purpose of this study since we are focusing on the stiffness differences between the '+' and '-' configurations. Since stiffness can be calculated as the second order derivative of the total elastic potential energy (equation 17) or as the first order derivative of the force (equation 18), there exist two distinct magnitudes of stiffness for the cell along the two corresponding branches of the force curve (i.e. the two stable configurations).

$$K = \frac{\partial F}{\partial X} = \frac{\partial F}{\partial \theta}\left(\frac{\partial X}{\partial \theta}\right)^{-1} \tag{19}$$

This is equivalent to the slope of the force deformation curve at the '+' and '-' configurations and therefore the two stiffness magnitudes are termed as 'K_+' and 'K_-'. This variable stiffness of the Miura unit cell has certain key advantages over other variable stiffness structures studied before. As mentioned previously, since the snap-through equilibrium condition requires the cell to stretch to its maximum dimensions, there is a reduced chance of unwanted switching between the stable configurations. Additionally,

since there are two branches of the force deformation curve within the same range of deformation, the two stable configurations with the variable stiffness magnitudes are closely matched in terms of external dimensions. Thus, the variable stiffness of the unit cell at its two stable configurations can open up a new range of applications which would not be previously attainable.

3.3 Variable elastic modulus of the cell

Since the unit cell is assumed to be a building block of an entire Miura solid, the effective elastic modulus of the Miura solid can also be calculated from the stiffness. Therefore, as the stiffness of the cell varies across its two stable configurations, the elastic modulus of the cell is also variable across those two bistable configurations. The elastic modulus as a function of the stiffness can be represented as:

$$E = \frac{KL}{A} \tag{20}$$

where, K is the stiffness of the cell,

L is the length of the element, and

A is the cross sectional area of the cell at the given configuration.

The variable elastic modulus of the cell can therefore be represented as E_-/E_+. The design scope of this study along with the experimental validation includes the variable stiffness and elastic modulus along the length of the unit Miura cell.

CHAPTER FOUR

MAPPING THE DESIGN SPACE OF THE UNIT CELL

Now that the origin of the bistability of the unit cell is established and the variable stiffness of the cell is derived, it is important to explore the design space to study the nature of bistability of the unit cell and how the variable stiffness can be programmed. This chapter investigates the range of the design parameters identified in Table 3.1 over which the unit cell is bistable and goes on to examine the correlation between these parameters and variable stiffness performance. This analysis is performed based on the variable stiffness along both length and width direction of the unit cell. The results from a comprehensive parametric study are also presented in this section. Since the variable stiffness of the unit Miura cell is characterized by the K_- / K_+ ratio, the input parameters from Table 3.1 are varied over a range to study their effect on this ratio. It is important to note that when each of the individual parameters are varied, the remaining parameters are the same as those given in Table 3.1. The selection of the range of variation of these design parameters takes into account preserving the unique folding geometry of the Miura cell. While identifying the key design parameters, the inputs are varied over a range where the cell is bistable so that the K_- / K_+ can be studied. These results can directly highlight the input parameters which have the maximum effect on the K_- / K_+ ratio and can help to select a set of design inputs to obtain a specific stiffness ratio between the two stable configurations of the unit cell. Table 4.1 provides the ranges over which each of the individual parameters are varied.

	Input Parameters	Range of Variation
Key Design Parameters	a_{II} / a_I	1 to 1.25
	b / a_I	0.4 to 2
	γ_I	35° to 85°
	$\theta°$	-70° to -40°
Secondary Parameters	k_{II} / k_I	7 to 20
	k_c / k_I	1 to 5

Table 4.1: Variation range of individual parameters

4.1 Design of the cell considering stiffness ratio along its length

4.1.1 Identifying the key design parameters

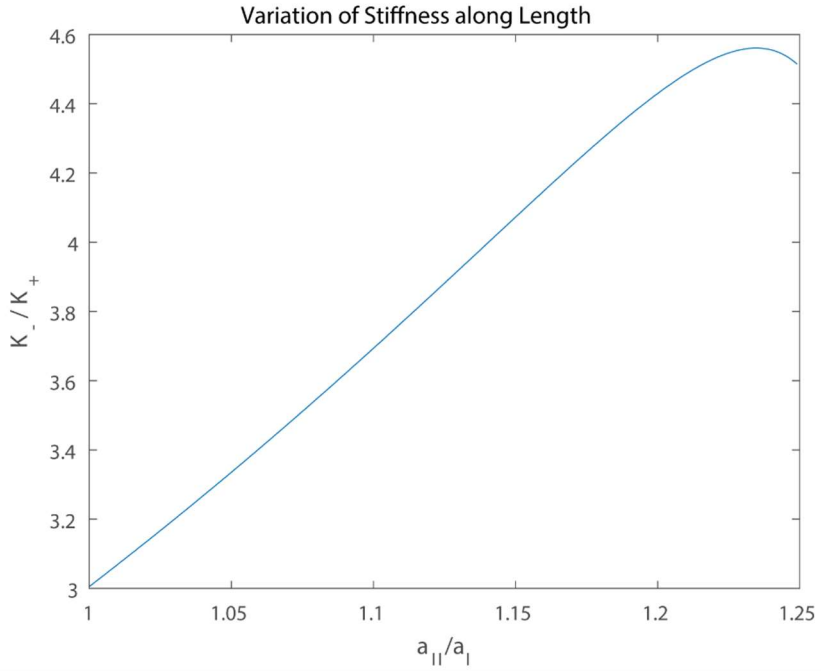

Figure 4.1 Variation of a_{II} / a_I along length

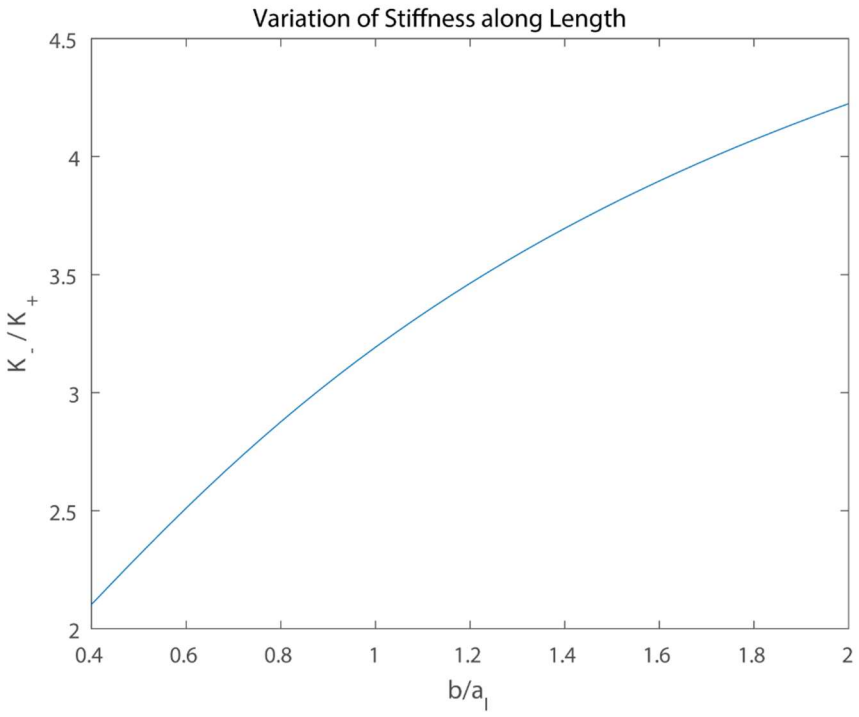

Figure 4.2 Variation of b / a_I along length

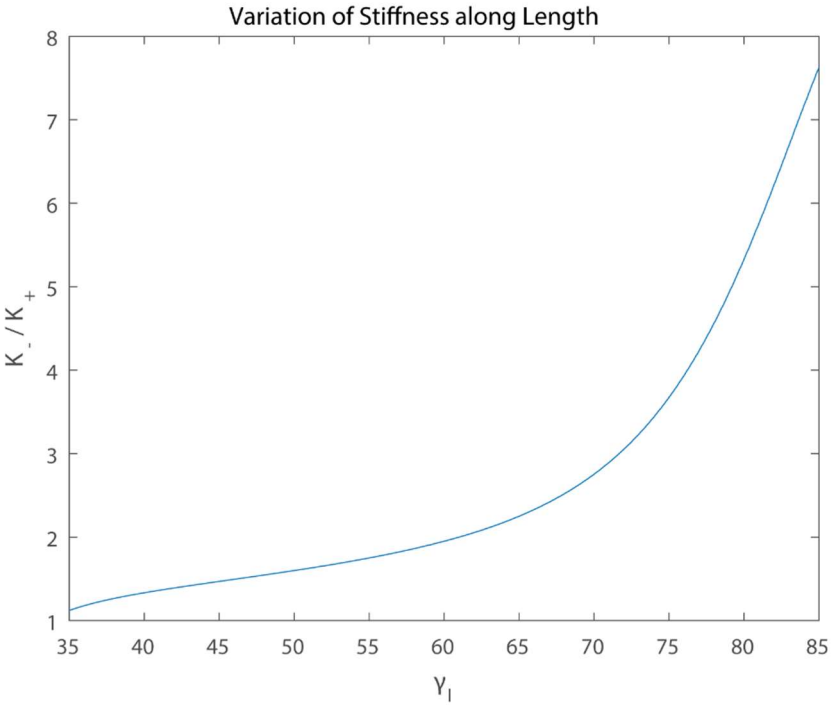

Figure 4.3 Variation of γ_I along length

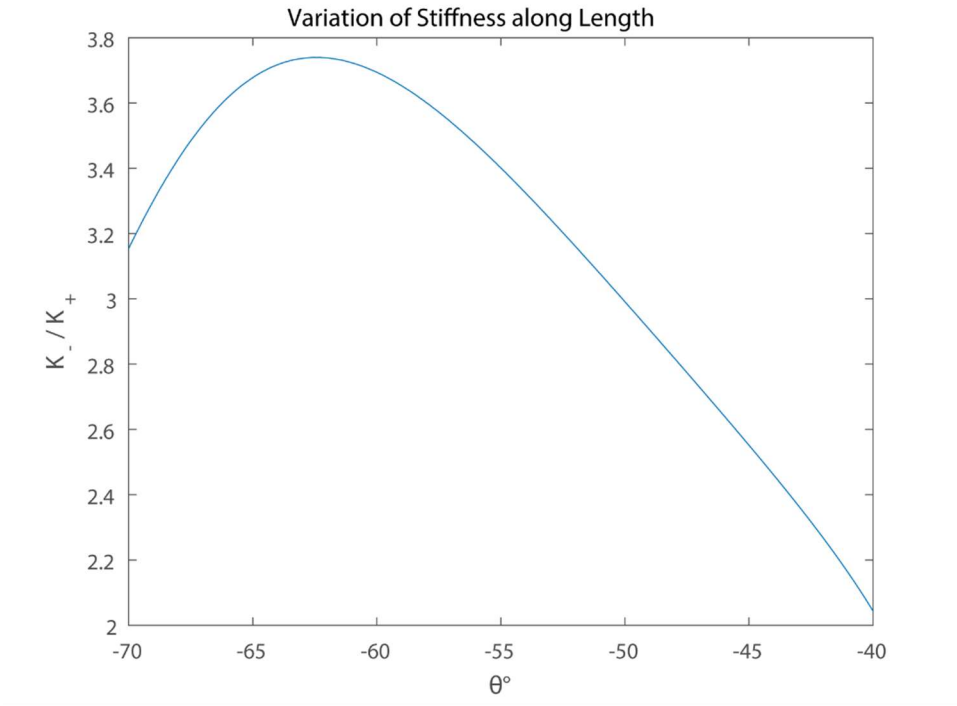

Figure 4.4 Variation of $\theta°$ along length

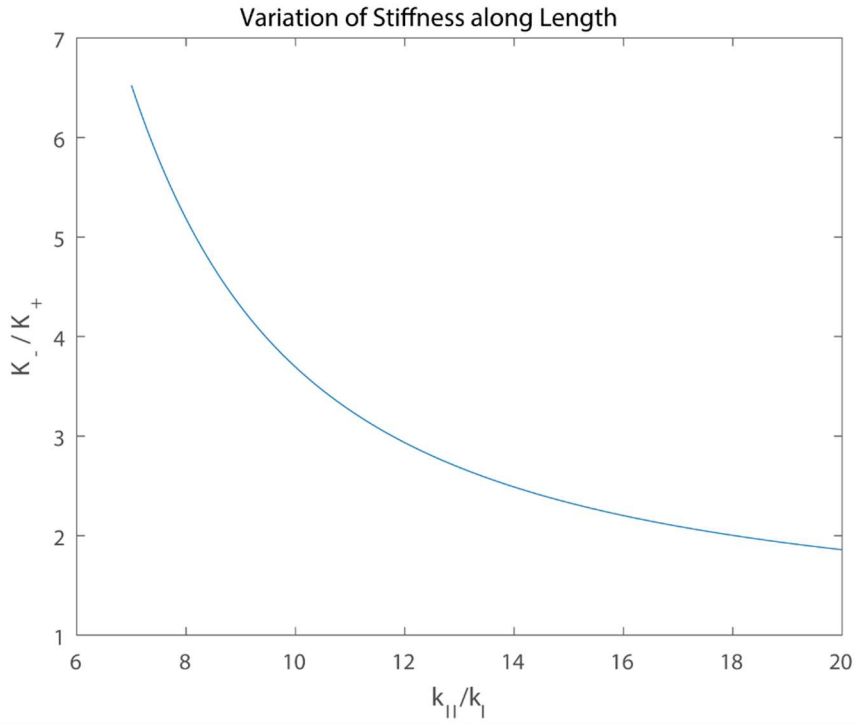

Figure 4.5 Variation of k_{II} / k_I along length

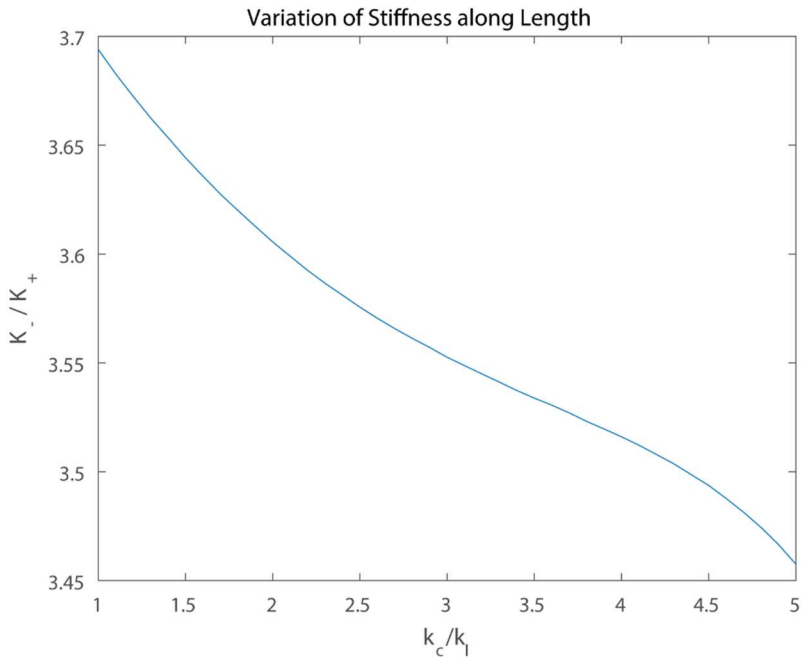

Figure 4.6 Variation of k_c / k_I along length

Figures 4.1 through 4.6 show the stiffness ratio K_- / K_+ along the length plotted over the range of all the individual parameters from of the unit cell. As identified in Table 3.1, the parameters are either geometric or material parameters. A preliminary analysis of the variable stiffness revealed that the K_- / K_+ ratio remains the same if the geometric parameters of the cell are scaled up or down uniformly. Due to this and also to provide a dimensional analysis, the crease length a_I is assumed to be constant and all the other facet lengths were plotted as a ratio to a_I. From the plots (figures 4.1 to 4.6), it is clear that the geometric parameters affect the K_- / K_+ ratio considerably. While the material parameter ratios (k_{II} / k_I and k_c / k_I) also contribute significantly to the stiffness ratio, it is more difficult to change these material parameters continuously because their values are limited to the particular material selection. It also worth noting that the k_{II} / k_I ratio has a minimum value

of 5 for the unit cell to be bistable. This result corroborates with the findings in [17] that increasing the crease stiffness ratio among the two Miura sheets makes the unit cell more bistable. Therefore, the geometric parameters can be identified as the key design parameters affecting the stiffness ratio of the bistable unit Miura cell while the material parameters are the secondary ones.

These design charts make it possible to achieve a desired K_- / K_+ ratio, i.e. one can use these design chart to tweak key design parameters while holding the others constant. It is also worth noting that the range of the key design parameters might have to be narrowed down in order to factor in manufacturability. For example, $\theta°$ is varied from -70° to -40° (Figure 4.4), however, when designing a physical prototype, it was noted that this stress free folding angle for the first stable configuration can be varied only within a narrower range (approx.. -65° to -50°) to ensure that the facets of cell have enough room to fold when switched to the second stable configuration. Due to the fact that while varying the stress free folding angle $\theta°$, there are further design implications restricting the freedom to tweak this parameter freely, it is not recommended as a key design parameter. Another key observation is that the K_- / K_+ ratio along the length of the cell is over 1 in all of the cases considered above which means that the stiffness magnitude of the '-' configuration is higher than that of the '+' configuration.

4.1.2 Studying the key design parameters

Once the key design parameters are identified, it is necessary to perform parametric studies and examine the achievable variable stiffness ratio. The interaction of these key parameters, two at a time, leads to the creation of a design space where the stiffness ratio K_- / K_+ can be studied. This design space is made more robust by extending the range of these key parameters (i.e. the range of variation of a_{II} / a_I is extended as 1 to 1.5) where the unit cell is not bistable (i.e. the mono stable region).

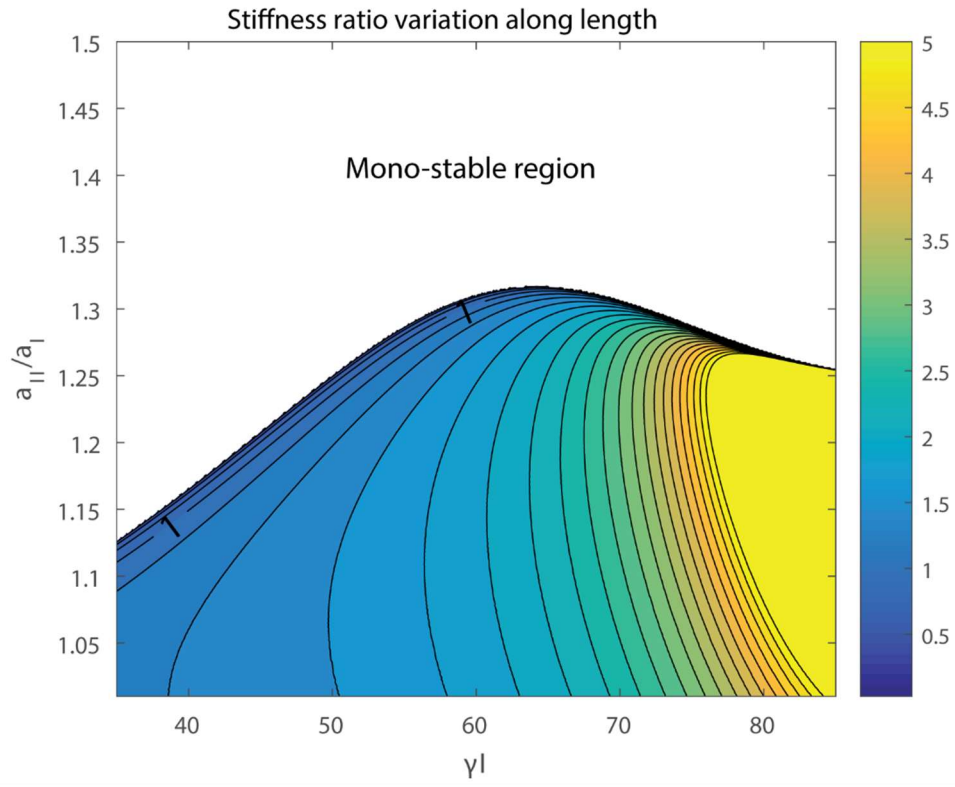

Figure 4.7 Variation of a_{II} / a_I and γ_I for stiffness ratio along length

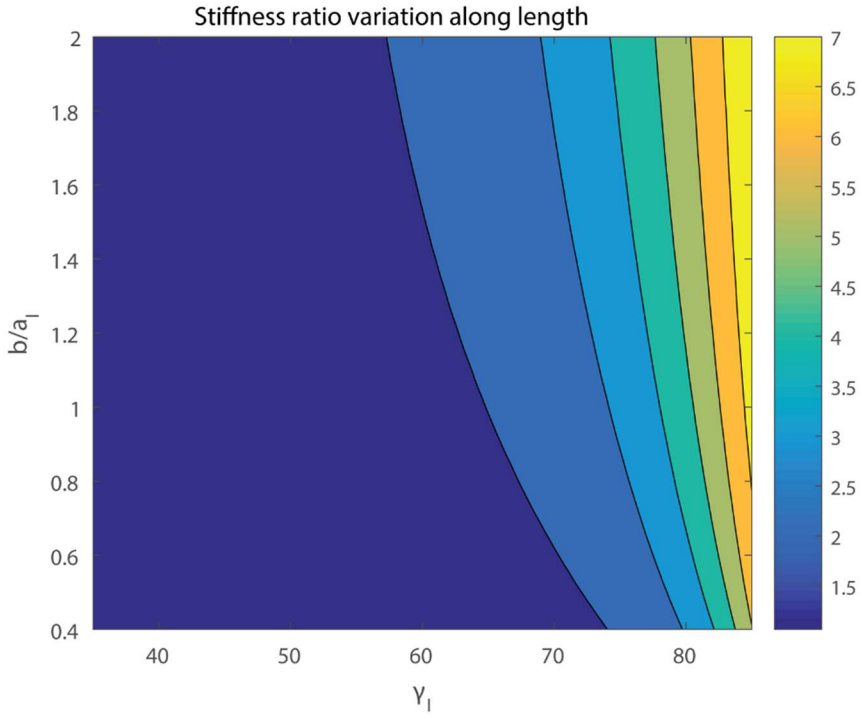

Figure 4.8 Variation of b / a_I and γ_I for stiffness ratio along length

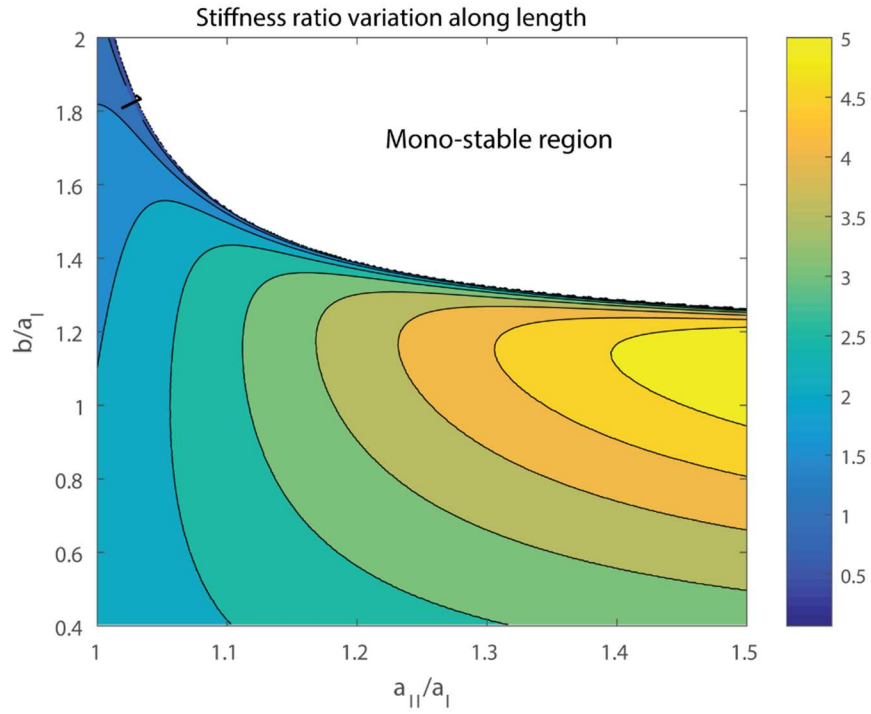

Figure 4.9 Variation of b / a_I and a_{II} / a_I for stiffness ratio along length

The above figures (4.7 to 4.9) show the design space mapped by simultaneously varying two key design parameters where the K_- / K_+ ratio is represented in as the colorbar. The white region in figures 4.7 and 4.9 represents the area where the unit Miura cell is mono-stable. The contour line where the K_- / K_+ is 1 is labelled at the boundary between the bistable and the mono-stable regions. This leads to the conclusion that there exists a design space where the K_- / K_+ ratio along the length is less than 1 which means that the stiffness of the '+' configuration is higher than that of the '-' configuration. However, it would be extremely difficult to select a design from this this particular region of the design space. Since the elastic modulus of the unit cell was identified as another property which can have targeted variable performance, the design space is also mapped for the modulus.

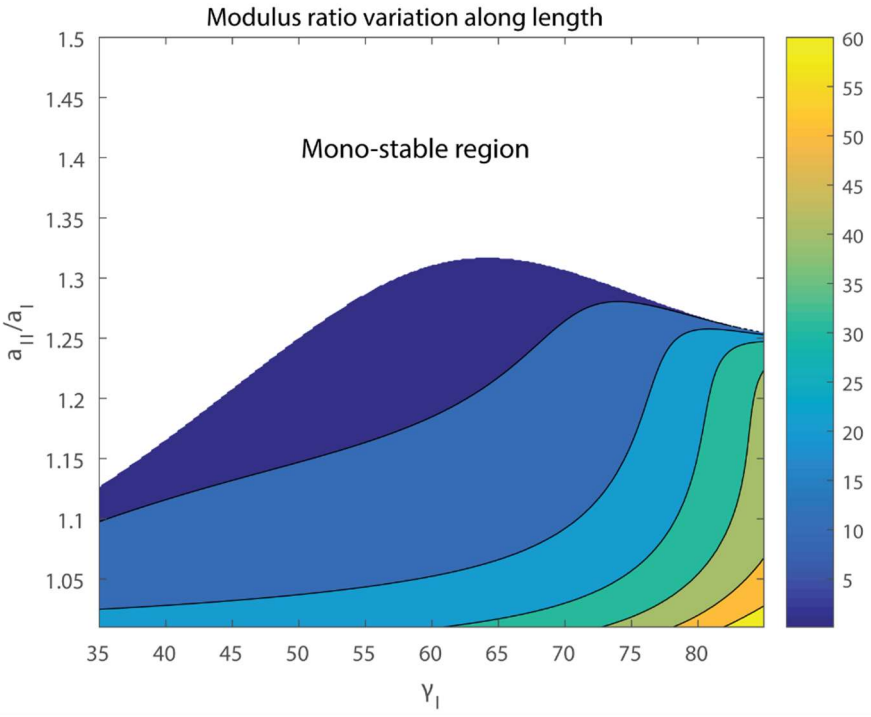

Figure 4.10 Variation of a_{II} / a_I and γ_I for elastic modulus ratio along length

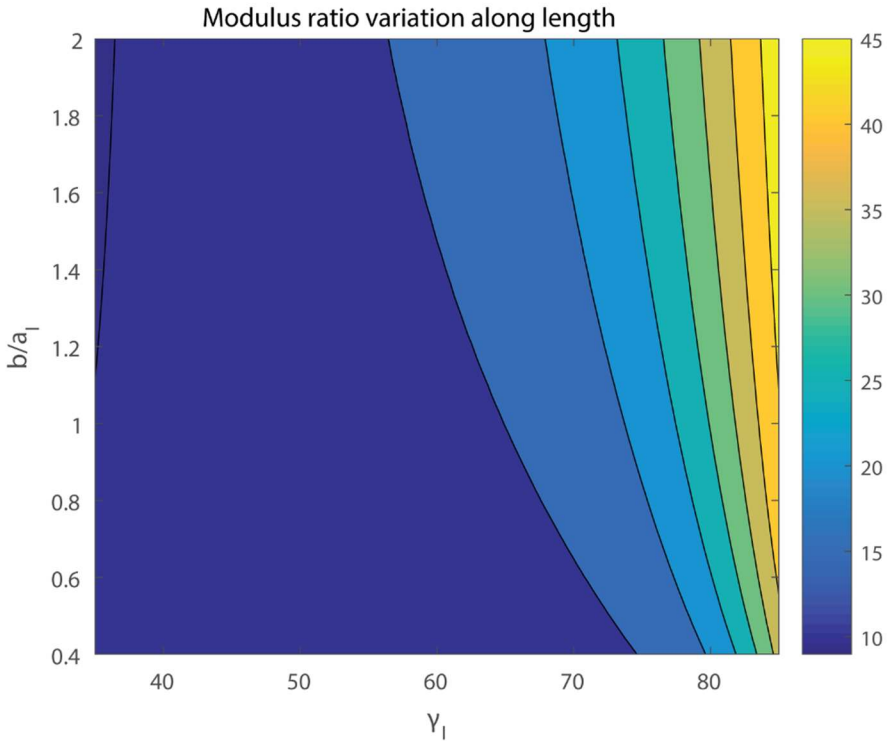

Figure 4.11 Variation of b / a_I and γ_I for elastic modulus ratio along length

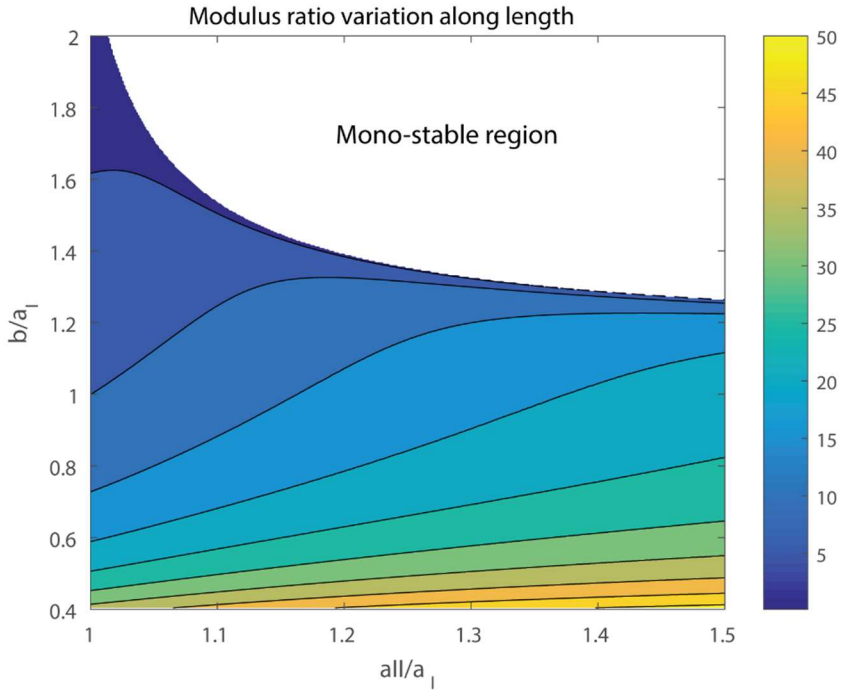

Figure 4.12 Variation of b / a_I and a_{II} / a_I for elastic modulus ratio along length

In the figures 4.10 to 4.12, the E_- / E_+ ratio is represented as the colorbar. From equation 20, since the elastic modulus E is directly proportional to the stiffness K, and inversely proportional to the cross sectional area A, the E_- / E_+ can be represented as

$$\frac{E_-}{E_+} = \left(\frac{K_-}{K_+}\right)\left(\frac{A_+}{A_-}\right) \tag{21}$$

The stiffness ratio K_- / K_+ from the contour plots is greater than 1. Also, the cross sectional area along the length for the unit cell in the '+' configuration is significantly higher than in the '-' configuration. Therefore, the E_- / E_+ ratios from the study of the dual key design parameters with the chosen design (Table 3.1) is significantly greater than 1 i.e. the elastic modulus of the '-' configuration is greater than that of the folded out '+' configuration. The sets of contour plots, in addition to mapping out the design space for the unit cell, also provide a systematic approach to pick a design for the cell based on targeted variable stiffness or elastic modulus.

4.2 Design of the cell considering stiffness ratio along its width

4.2.1 Identifying the key design parameters

Since the unorthodox nature of the bistability of the Miura-ori design is observed both along the length and width of the cell, the design space is studied for both the cases. The same procedure is followed for the study as in the case of the length and the range of variation of the parameters are again from Table 4.1.

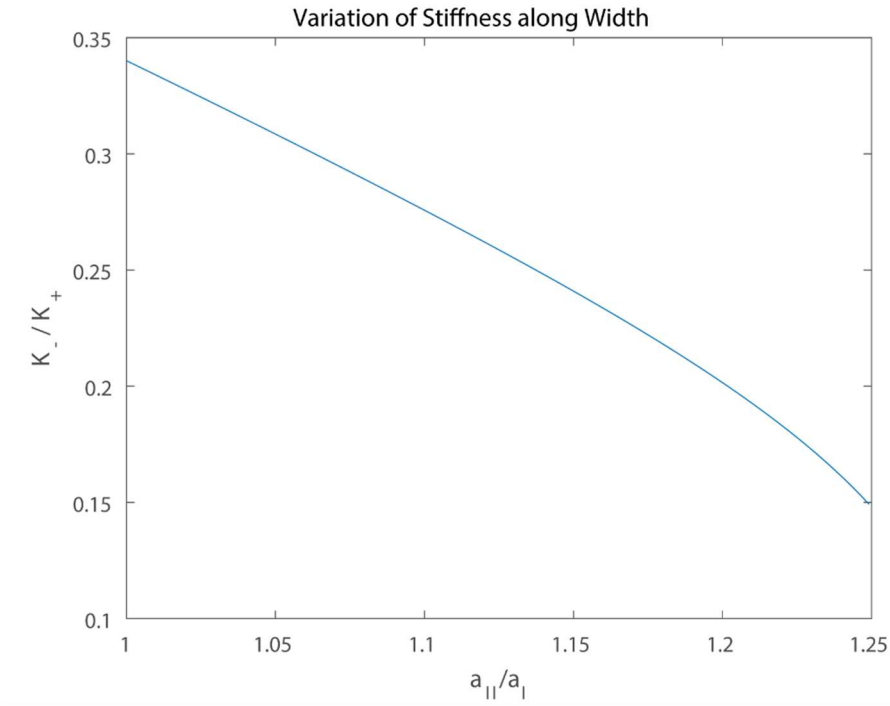

Figure 4.13 Variation of a_{II} / a_I along width

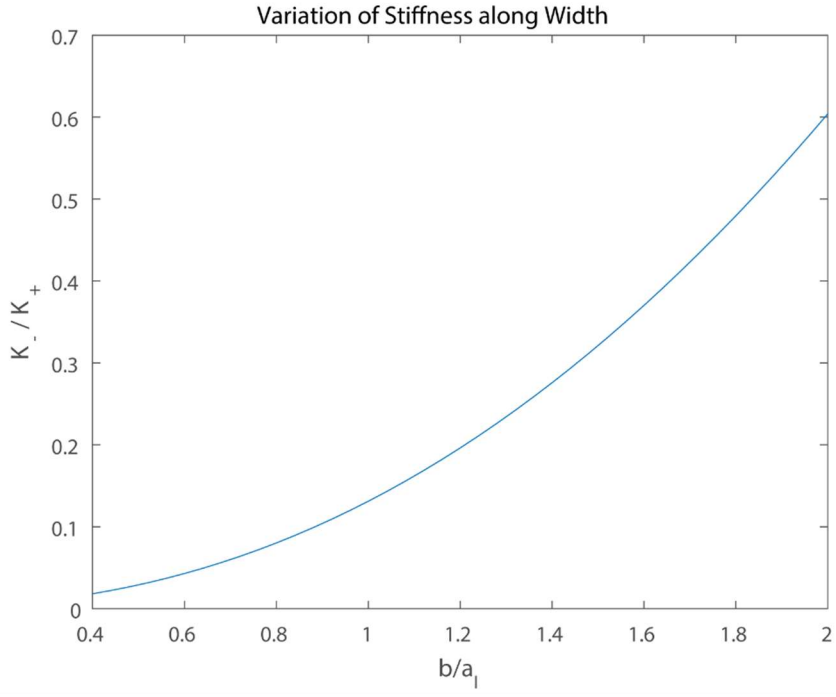

Figure 4.14 Variation of b / a_I along width

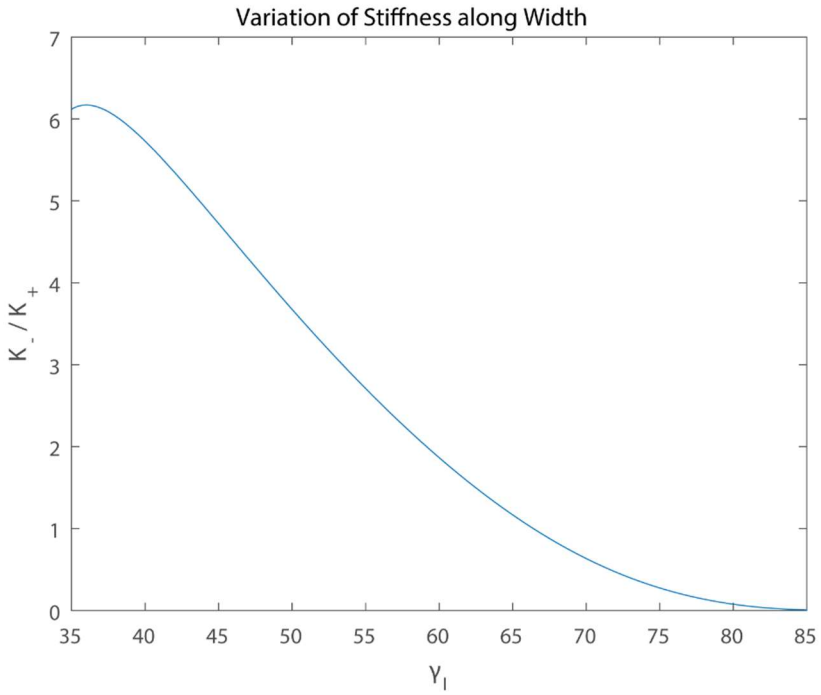

Figure 4.15 Variation of γ_I along width

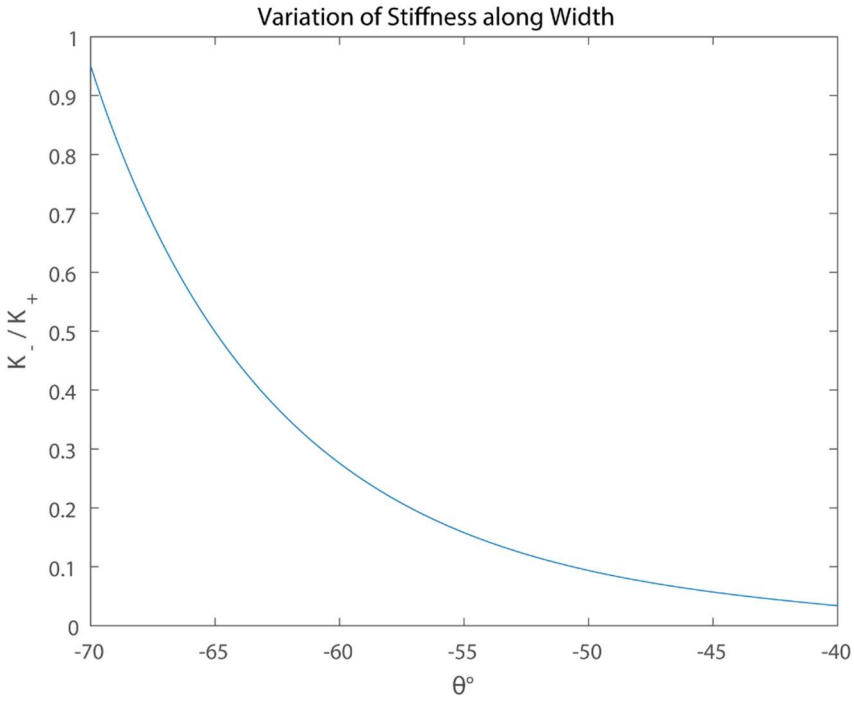

Figure 4.16 Variation of $\theta°$ along width

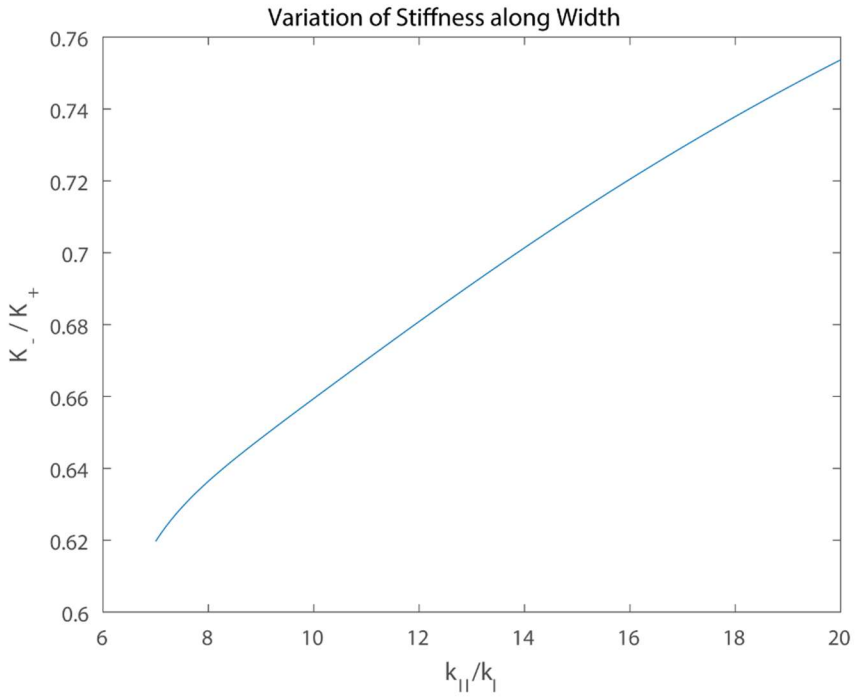

Figure 4.17 Variation of k_{II} / k_I along width

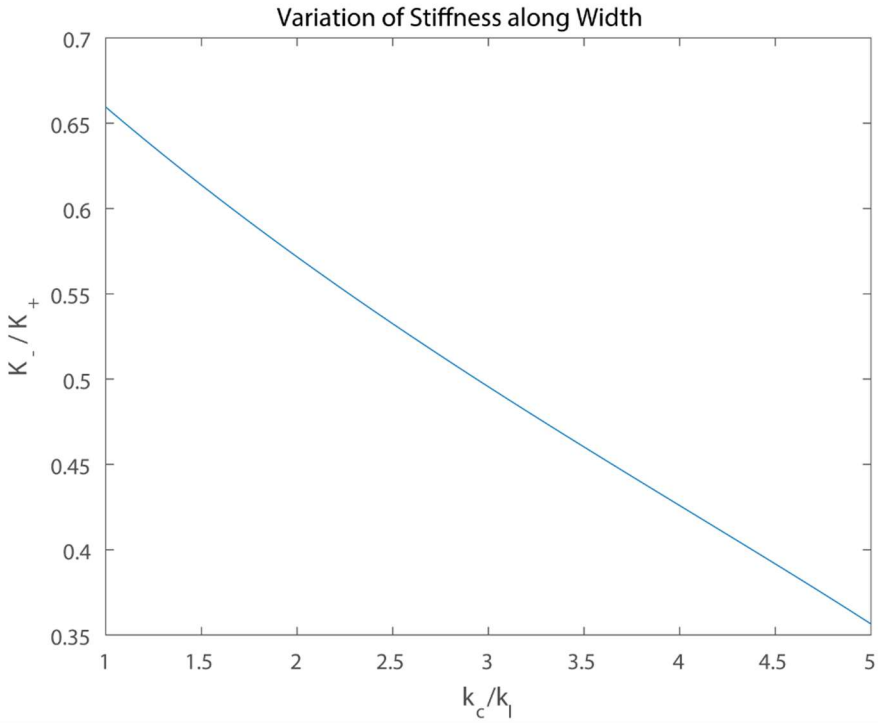

Figure 4.18 Variation of k_c / k_I along width

The first noticeable difference for the K_- / K_+ ratio along the width as compared to that along the length is that the ratio is less than 1 for all the design inputs with the exception of γ_I. The K_- / K_+ ratio observed over the range of variation of γ_I shows that it is less than 1 only for $\gamma_I > 60°$. This leads to the conclusion that along the width of the unit Miura cell, the stiffness magnitude of the '+' configuration is generally greater than that of the '-' configuration. Along the width of the unit cell, the parameter ratios a_{II} / a_I, b / a_I and the angle γ_I are still considered as the key design inputs. Therefore, similar to the design case along the length of the cell, the targeted K_- / K_+ ratio can be achieved by choosing the appropriate key design parameters while the material properties are dependent on the choice of material used for the prototype.

4.2.2 Studying the key design parameters

The parametric study of the key inputs is performed again, this time to study the effect they have on the K_- / K_+ and E_- / E_+ along the width direction of the unit cell. The bistable space remains the same along the width of the cell but the variable stiffness and elastic modulus in that bistable region show completely different performance than along the length. This makes the Miura cell capable of being bistable in three dimensions, and bistability along two of these dimensions can be harnessed to design this cell with such unique and unconventional mechanical properties.

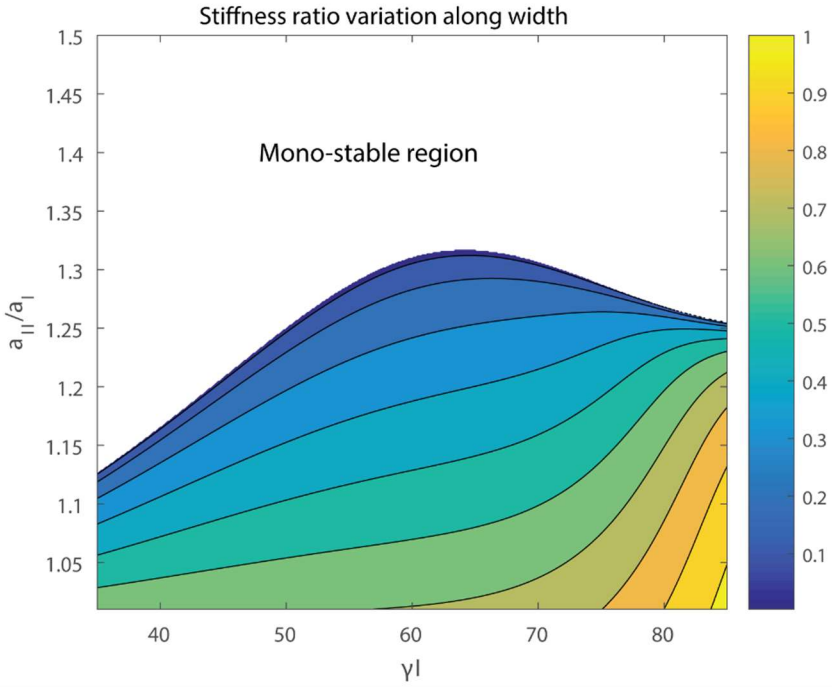

Figure 4.19 Variation of a_{II} / a_I and γ_I for stiffness ratio along width

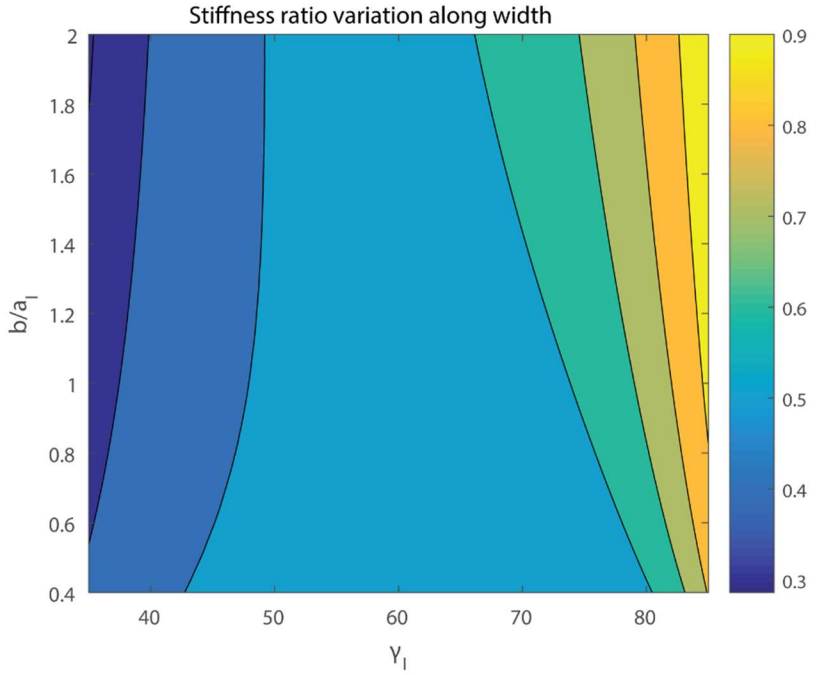

Figure 4.20 Variation of b / a_I and γ_I for stiffness ratio along width

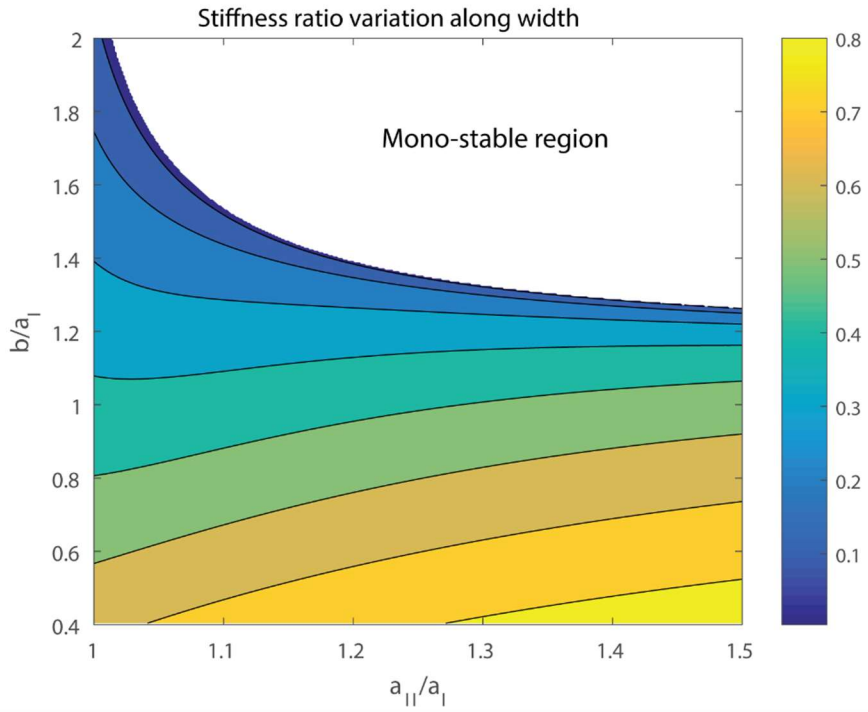

Figure 4.21 Variation of b / a_I and a_{II} / a_I for stiffness ratio along width

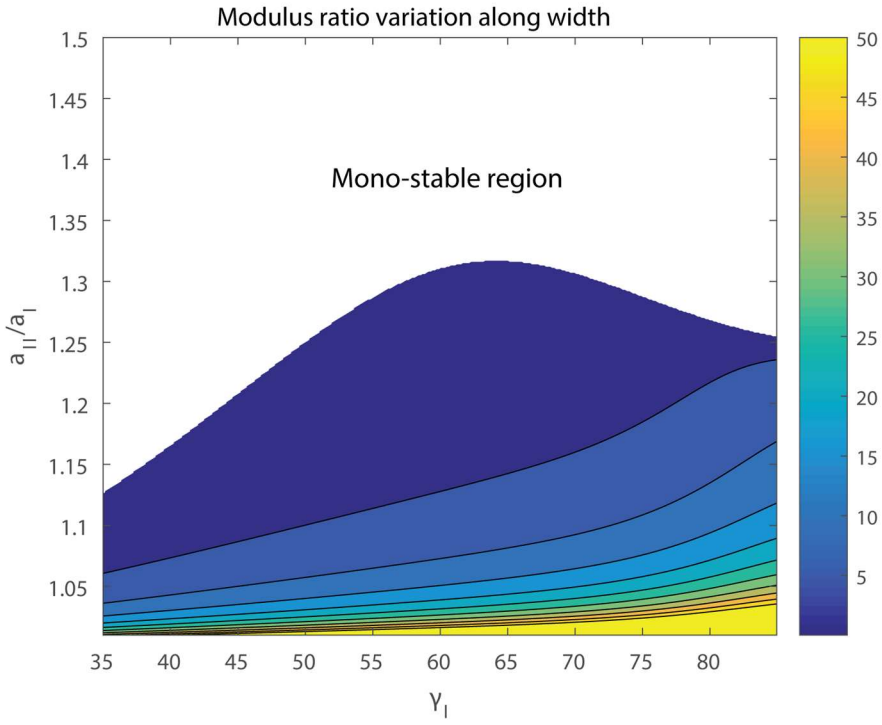

Figure 4.22 Variation of a_{II} / a_I and γ_I for elastic modulus ratio along width

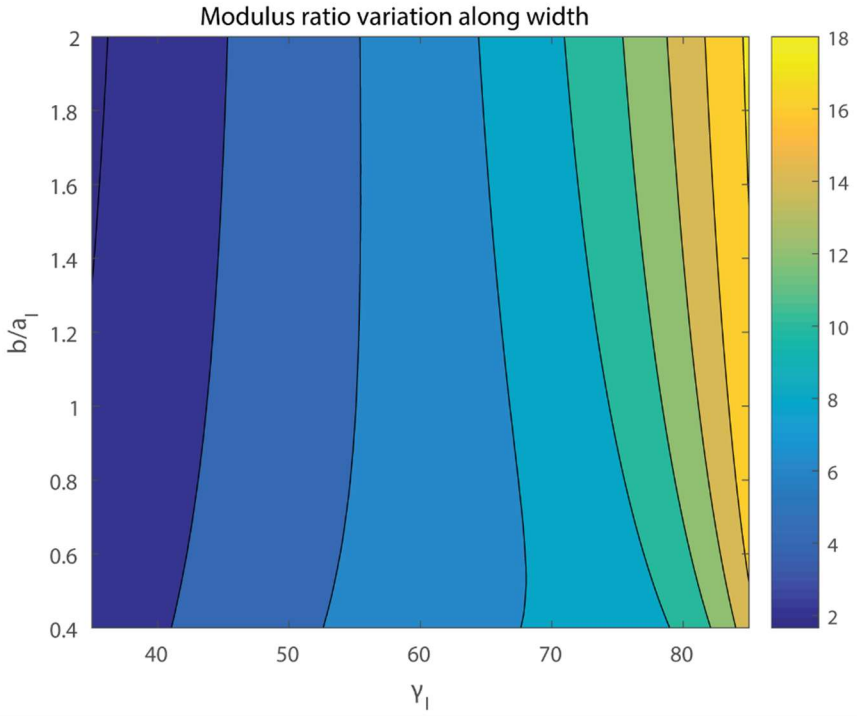

Figure 4.23 Variation of b / a_I and γ_I for elastic modulus ratio along width

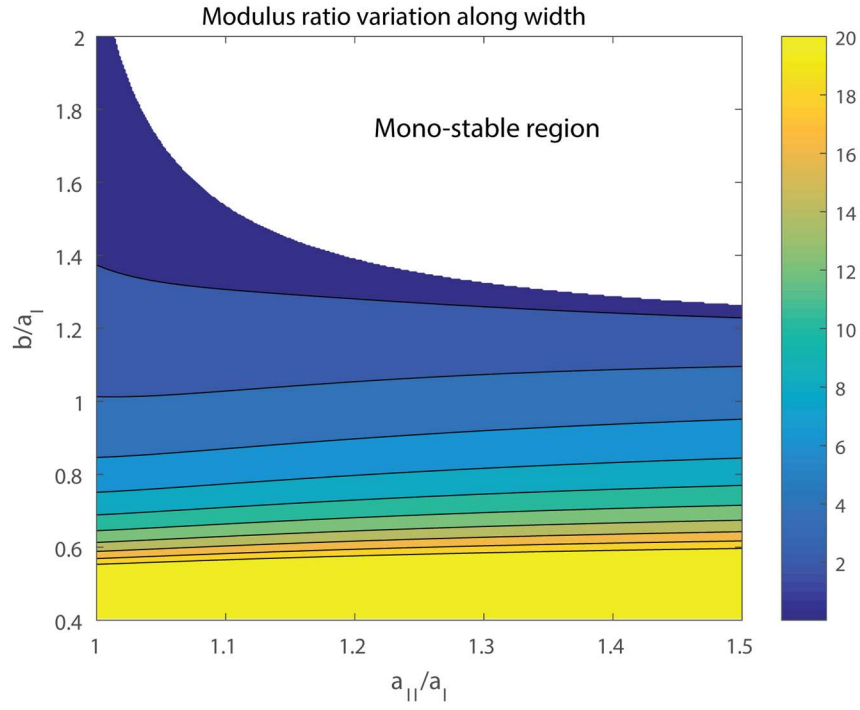

Figure 4.24 Variation of b / a_I and a_{II} / a_I for elastic modulus ratio along width

All the design plots (figures 4.19 through 4.24) show the design space for the set of input parameters from Table 3.1. It is seen that in the given design space, the '-' configuration is less stiff than the '+' configuration over the bistable region along the width direction of the cell. Additionally, the elastic modulus of the folded in '-' configuration is again greater than that of the folded out '+' configuration.

4.3 Summary of the parametric design study

The previous subsections in this chapter present a comprehensive study of the design space of the bistable unit Miura cell with the chosen design inputs from Table 3.1. All of the information and design plots presented help to identify a suitable set of design parameters for the unit cell with a specific targeted performance in mind. A further important inference made during the parametric study to map the design space was that the folding angle $\theta°$ significantly affects the bistability of the cell and also the K_- / K_+ and E_- / E_+ ratios. However, a limitation of this angle is that there is a very specific narrow range of values that can be exploited to actually fabricate a unit cell using an engineering material. The design plots shown in the previous section use $\theta° = -60°$ from the design inputs table (table 3.1). This value is deemed appropriate so that the fabricated unit cell has enough space to fold in the facets in the '-' configuration. The design space and the performance characteristics of the variable stiffness and elastic modulus change completely with a change in this stress free folding angle. To further illustrate this point, some further sample design plots are included in Appendix A with $\theta° = -55°$ which show how the bistable performance area of the cell can change. In the process of selecting a design for the cell,

the findings from this research indicate that a suitable value of $\theta°$ should be identified based on the manufacturability and folding of the prototype and then a design space can be built around this selected value.

The final part of the design analysis is to calculate the K_- / K_+ and E_- / E_+ ratios for the set of design parameters from Table 3.1. The Matlab scripts used to calculate the stiffness and elastic modulus ratios are shown in Appendix B. These are summarized below:

Performance metric	**Ratio along Length**	**Ratio along Width**
$\boldsymbol{K_- / K_+}$	3.68	0.66
$\boldsymbol{E_- / E_+}$	14.94	10.99

Table 4.2 Variable performance metrics for the chosen design of unit cell

The stiffness and elastic modulus ratios from Table 4.2 can be used to compare against the ratio obtained by experimentally testing the unit cell prototypes.

CHAPTER FIVE

PROTOTYPE DESIGN AND EXPERIMENTAL RESULTS

Once the design of the bistable unit Miura cell is studied along with the variable stiffness and elastic modulus, the second half of this research aimed at successfully fabricating a prototype and obtaining experimental results. Two distinct fabricating techniques for the manufacturing a prototype of the unit Miura cell can be devised. The first would be to manufacture the facets using sheet metal and laser cutting, water-jet cutting or other similar methods and to use torsional springs which would act as hinges. However, it is obvious this method of fabrication will require assembling the different facets and hinges to form the cell. While this might be feasible for the fabrication of a single cell, it would be impractical when the fabrication of an entire Miura solid is considered consisting of many such unit cells. Therefore, another fabrication technique is necessary which can be holistically extended to also manufacture entire structures and not just a unit cell. The solution to this is found in the form of 3D printing. 3D printing has found applications in the fabrication of one-of-a-kind, custom parts which are difficult or even impossible to manufacture using conventional manufacturing techniques. It has found applications in the electronics, medical and aerospace industries to name a few [22]. Using 3D printing ensures that the unit cell, or the Miura structure can be printed as a whole without the need for any complicated or tedious assembly. Since the design of the cell is bistable and the printed prototype has to be able to snap between the two stable configurations, a suitable material is also required which can facilitate this requirement. Again, a solution is readily available in the form of flexible materials which are being used

in a host of different types of 3D printing techniques. These flexible materials have applications in deformable electronic sensors which can also be wearable and even soft robotics [23] and more commonly in cell phone and tablet covers. These materials, along with the 3D printing technology, are adequate to fabricate Miura structures. The research presented in here used a couple of different types of 3D printing along with different materials to fabricate prototypes of the unit Miura cell. The CAD model of the unit cell with its cross sectional area are shown in Figures 5.1 and 5.2.

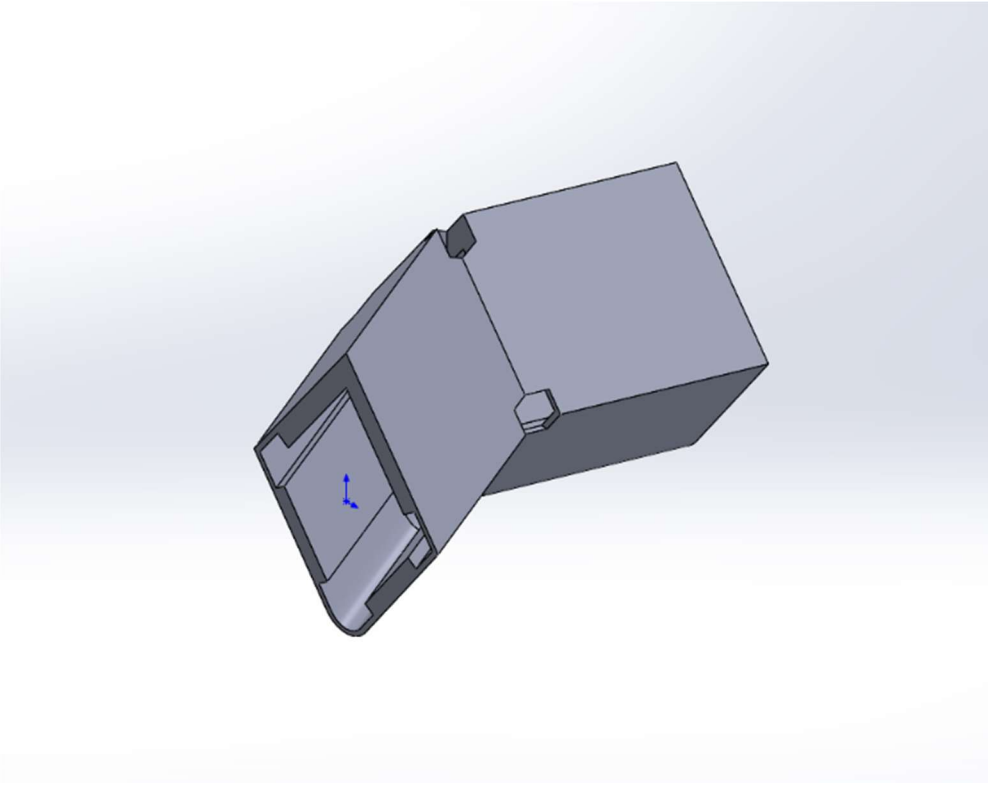

Figure 5.1 CAD model of the unit cell

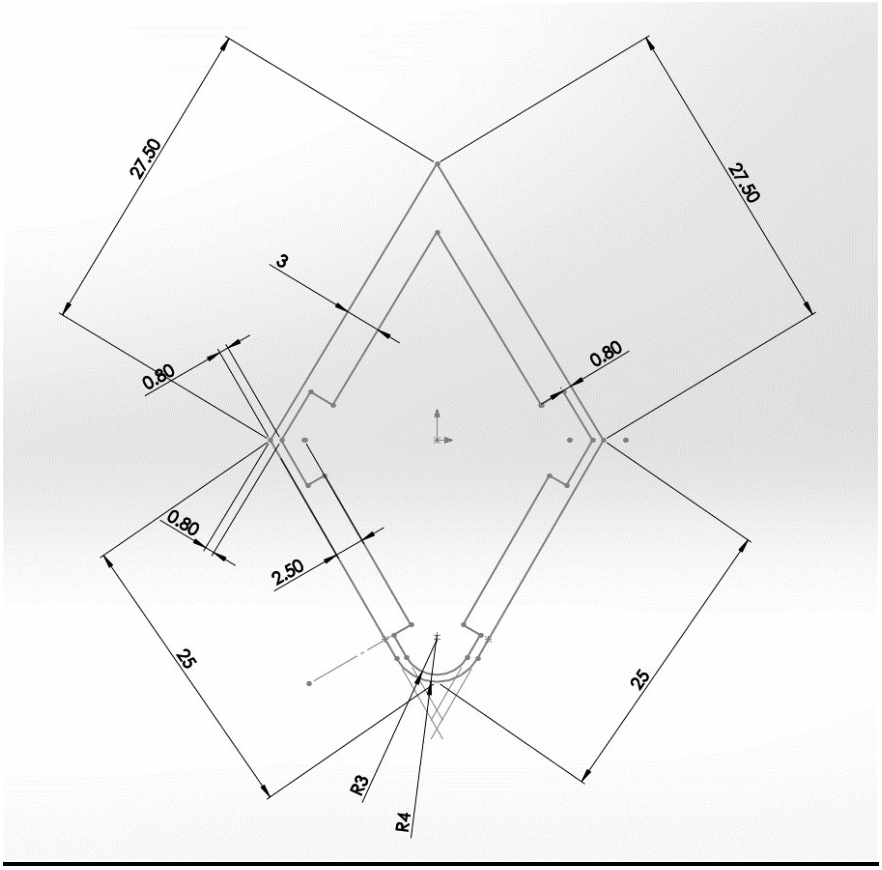

Figure 5.2 Cross sectional area of the unit cell

The one limitation of the design study is that in all of the analyses, the thickness of the Miura cell is not considered. However, when a prototype is designed, the thickness of the facets and the creases are important geometric inputs. The crease thickness is crucial in dictating the difference in the crease stiffness per unit length (k_I, k_{II} and k_c). Since the creases are assumed to be similar to flexural hinges, crease stiffness is proportional to the cube of the crease thickness.

$$\frac{k_{II}}{k_I} \propto \left(\frac{t_{II}}{t_I} \right)^3 \tag{22}$$

Therefore, the crease of the smaller Miura sheet (k_I) and the shared crease (k_c) are both 0.8 mm thick since $k_I = k_c$ from the design table 3.1 while the larger Miura sheet crease is thicker. The thickness of the facets were estimated to ensure that the facets could fold smoothly into the '-' configuration. Figure 5.1 shows the holes which are cut out in the vertices of the cell, this is done to remove any stress concentrations on these vertices when the cell is folded. This chapter further goes on to describe the two version of the unit cell design and highlights the experimental results from the 3D-printed prototypes.

5.1 Design of prototype version 1

The first prototype was printed using a Fused Deposition Modeling (FDM) printer and the material used was Thermoplastic Polyurethane (TPU), which is a common flexible filament for FDM printers. The printer used for this prototype is a Lulzbot Taz 5 and the TPU material is made by GizmoDorks. The technical characteristics for this material advertised by the manufacturer are as follows:

Hardness	98 Shore A
Elongation at Break	600% Strain
Tensile Strength	11600 psi
Density	1.25 g/cm³

Table 5.1 TPU material characteristics

The maximum strain at failure of this material shows the amount of flexibility it can achieve which is suitable for the design requirements of the bistable Miura cell. Using this material, the critical print specifications used to print this version of the prototype are listed in Table 5.2.

Extrusion Temperature	220 °C
Heated Bed Temperature	90 °C
Print Speed	10 mm/sec
Layer Height	0.15 mm
Support Type	Overhangs with angle less than 60°
Retraction Speed	50 mm/sec

Table 5.2 Print Specifications for prototype v.1

In order to obtain a consistent material extrusion and also a smooth finish, a fairly high extrusion temperature of 220 °C and a relatively low print speed of 10 mm/sec were used for printing this prototype. Because of the slow extrusion speed, over-extrusion is a distinct possibility and in order to avoid that, a high retraction speed of 50 mm/sec was set as shown in Table 5.2. These specifications in Table 5.2 were fine-tuned after printing different iterations of the same model of the unit cell. Figures 5.3 and 5.4 show this printed prototype.

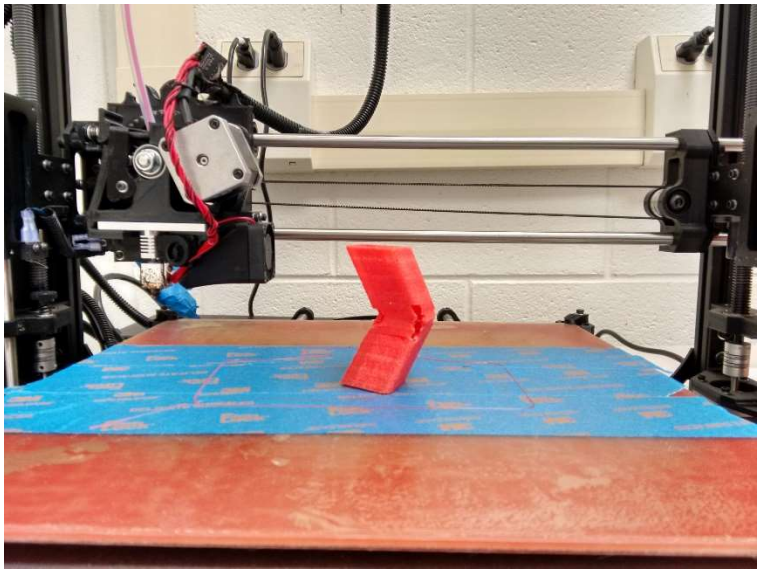

Figure 5.3 Snap-shot of the printed prototype on the printer bed

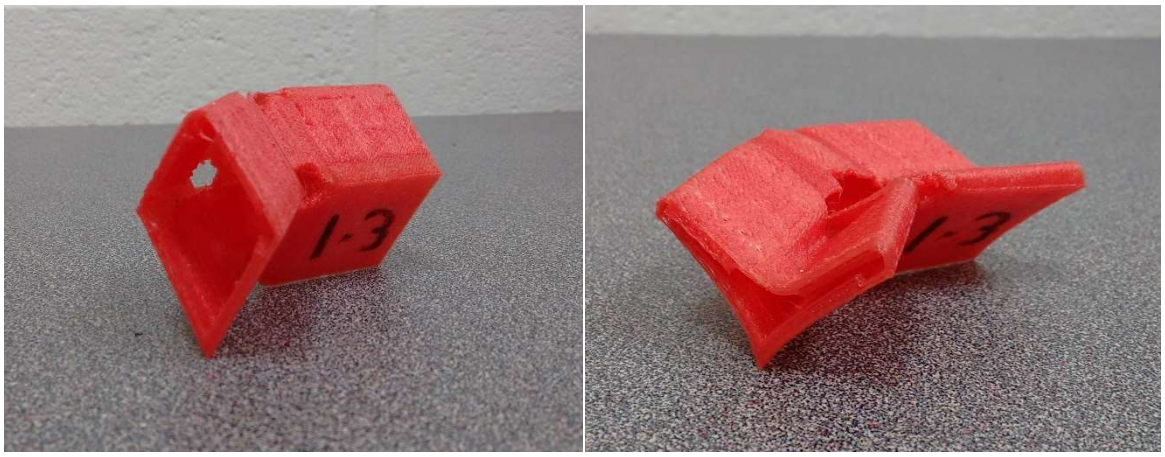

Figure 5.4 '+' and '-' configurations of the bistable printed prototype v.1

5.2 Design of prototype version 2

A better material was identified in the design of this second prototype which is capable of printing a cell with a stronger bistability. The snapping motion between the two stable configurations was more pronounced in this version. The 3D-printing process used

for this second version was Selective Laser Sintering (SLS) with a powdered elasto-plastic material available from Shapeways, a custom 3D-printing service provider. This second prototype was identified as a better option in terms of the bistability and the folding motion of the printed part and subsequently, the experimentations for calculating the stiffness were done on this version. Figure 5.4 shows the printed part of this design version.

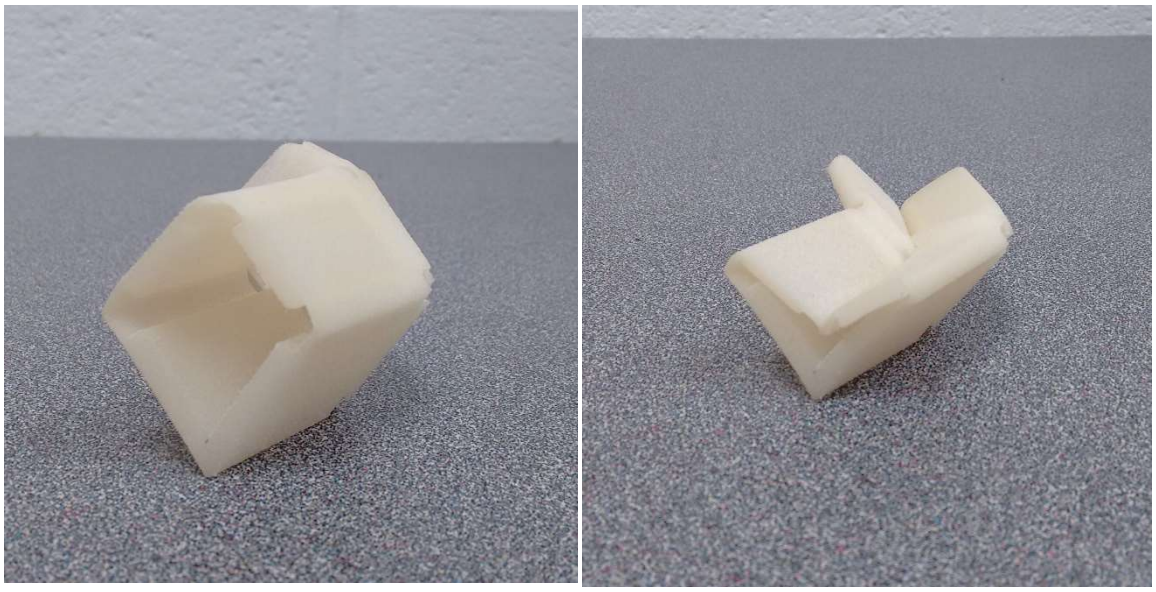

Figure 5.5 '+' and '-' configurations of the bistable printed prototype v.2

5.3 Experimental Results

5.3.1 Test Procedure

In order to calculate the stiffness of the unit Miura cell at its two stable configurations, a compression test was performed on it and the force-displacement data was collected. The slope of this force-displacement curve was the stiffness of each of the two stable configurations from which the experimental K_- / K_+ ratio was calculated. The machine used for this compression test was an ADMET eXpert 5000 modular testing machine.

The test setup was designed to ensure that the compressive force was retracted after the test prototype was displaced by 2.5 mm. This displacement magnitude ensured that the geometry of the unit cell remained close to the stable configurations and did not further deform it. Figure 5.6 below shows the '+' and '-' configurations under the test setup.

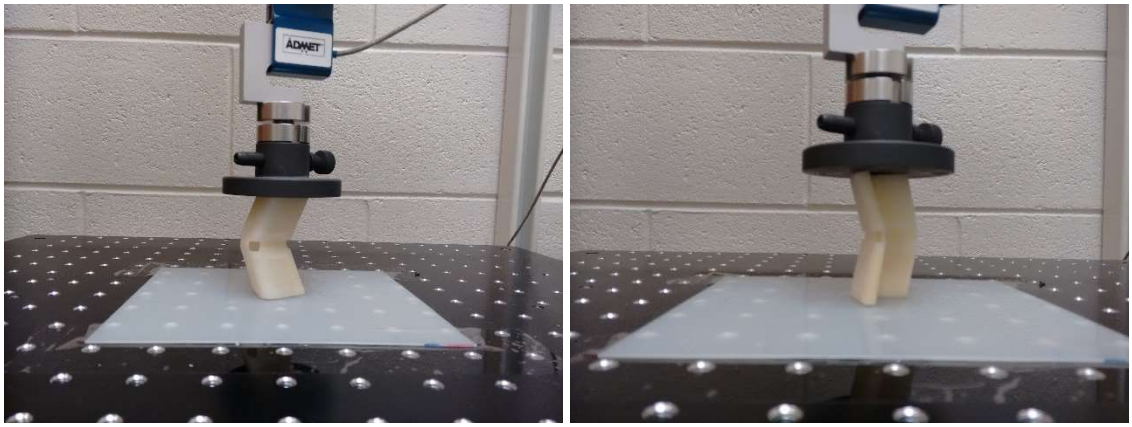

Figure 5.6 '+' and '-' configurations of the v.2 unit cell prototype in the test apparatus

5.3.2 Test Results for stiffness ratio

The test procedure was used to run the experiments on both the stable '+' and '-' configurations of the v.2 unit cell design described in section 5.2. Ten force-displacement readings were recorded for each of the stable configurations. These force-displacement curves shown in figure 5.7 were linear fitted and their slope resulted in the stiffness of the unit cell at a particular specific configuration. The data from these tests are presented below in Table 5.3.

Test #	K_+ **(N/m)**	K_- **(N/m)**
1	7064	7109
2	6839	9736
3	6901	5404*
4	6776	5951*
5	6792	8178
6	6871	8576
7	6866	7398
8	6767	10061
9	6861	7978
10	6804	8939
Average	**6854**	**8497**

Table 5.3 Test Results of v.2 unit cell

There are certain considerations that were made during the analysis of these test results. These are listed below:

- The K_+ and K_- values from the results (Table 5.3) are not cross-checked with those from the theoretical calculations (Table 4.2) since the theory assumes k_I = 5 N (Table 3.1) and the material specifications for the elasto-plastic used in the v.2 design are not available. However, this does not adversely affect this work since the objective here is to study the K_- / K_+ ratio and not the stiffness magnitudes themselves.

- The theory also considers k_{II} = 50 N (=10*k_I) from the design parameters table 3.1. However, again since the material properties are not available, the design of the creases is related to their thickness as explained in equation 22. Because of manufacturing considerations of 3D-printing of the model having a minimum wall thickness of 0.8 mm and to make the unit cell bistable, the crease thickness are t_{II} = 3 mm and t_I = 0.8 mm. Therefore, the ratio of the crease stiffness per unit length, from equation 22, is estimated to be (k_{II} / k_I) = 52. Again, the absolute values of the crease stiffness per unit lengths do not have any effect on the theory or the test results since the ratio of crease stiffness among the two Miura sheets dictates the bistability of the unit cell.
- Since the slope of force-displacement curves from the test results provide the stiffness, the curves are linear fitted. The 3rd and 4th values of K_- from Table 5.3 are considered as outliers since their force-displacement curves were highly non-linear. These particular readings are also not considered while calculating the average.

After taking the above considerations into account, the theoretical K_- / K_+ ratios are re-calculated and the average of the results from Table 5.3 are compared against them as shown in Table 5.4. The average force-displacement curves for the '+' and '-' configurations from Table 5.3 are illustrated in Figure 5.7.

	Revised Theoretical	**Experimental**
K_- / K_+ ratio	1.24	1.23

Table 5.4 Comparison of test results against theoretical results

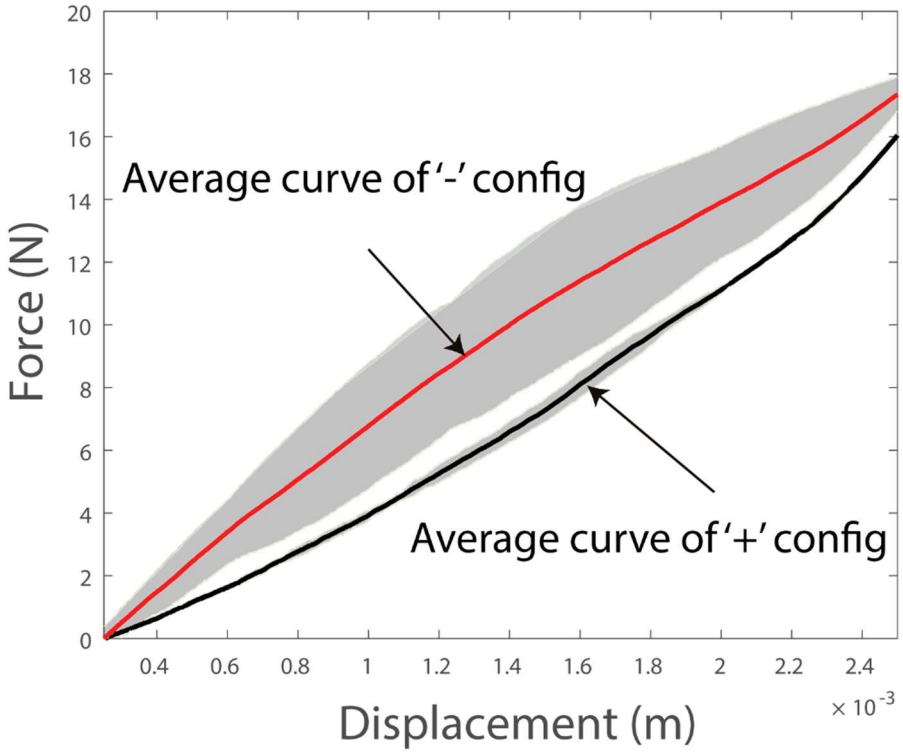

Figure 5.7 Averaged experimental force-displacement curves

Table 5.4 shows that the test results correspond well with those expected from the theoretical analysis. The averaged force-displacement curves for the '+' and '-' configurations in figure 5.7 show that a good estimation of stiffness (slope) can be achieved by using a linear fit on both the curves. While performing the compression cycles on the unit cell prototype, it was observed that they adhere to the expected folding motion under the compressive forces. These test results help in providing a valuable proof-of-concept and help validate the study. These results can help pave the way for future design of bistable unit Miura cells based on a targeted variable stiffness performance and they can even be extended to structures with multiple such unit cells.

CHAPTER SIX

ASSEMBLING THE UNIT CELLS INTO A MIURA CHAIN

After studying the bistable unit cell, this chapter explains how these cells can be assembled into a Miura meta-structure which possesses multiple stable configurations. Since the unit cell is identified as the basic building block of the Miura structure, and if each unit cell is assumed to be identical, the properties of the multi-stable structure can be studied to show how it can display programmable stiffness. The analysis of such a multi-stable Miura structure shows that the vertical stacking of the cells leads to programmable stiffness along this vertical chain. Horizontally stacked cells do not possess variable stiffness, the magnitude of the stiffness is identical for every horizontal row. Thus, this work focuses on the study of the programmable stiffness achieved by stacking the unit cells vertically. This chapter briefly discusses how the unit cells can be assembled to form such a vertical chain which has multiple stable configurations and programmable stiffness.

Analysis of a Miura Chain

The unit cells can be stacked together to form a Miura chain. This section explains how the multi-stable configurations of such a Miura chain can display programmable stiffness. It is assumed that each unit cell is identical and '*m*' such identical unit cells are assembled into a chain. Figure 6.1 shows the CAD model of chain with $m = 2$ i.e. two unit cells stacked vertically on top of each other. Since each of these two cells is bistable i.e. have two stable configurations, the dual cell chain will have a total of 4 (2^{m}) stable

configurations. This dual cell chain was 3D-printed and the 4 stable configurations are shown in Figure 6.2.

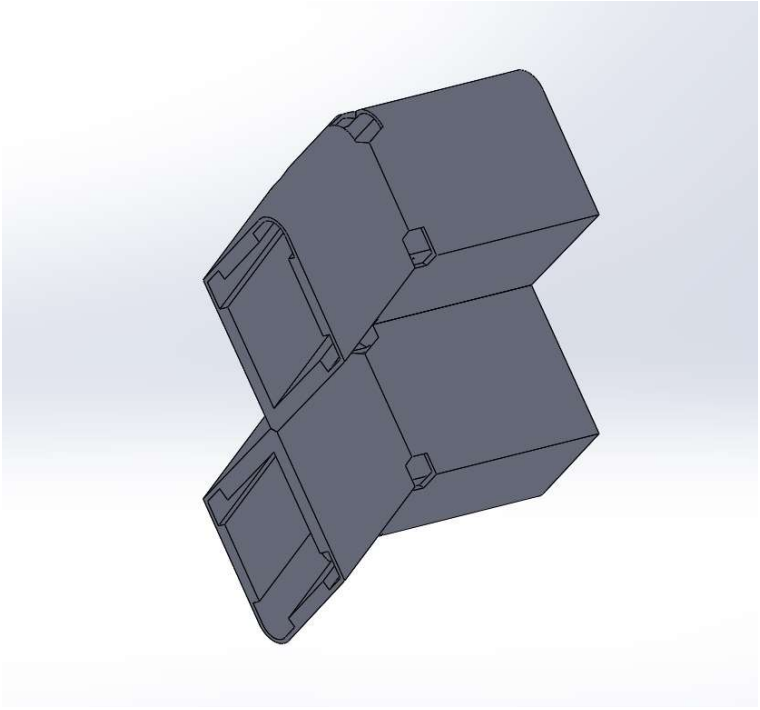

Figure 6.1 CAD model of a dual cell chain

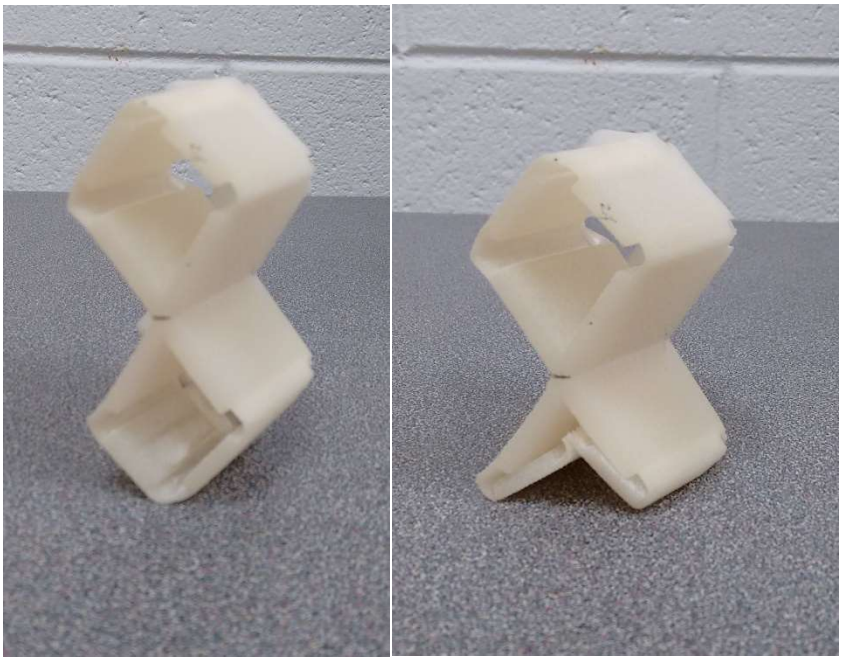

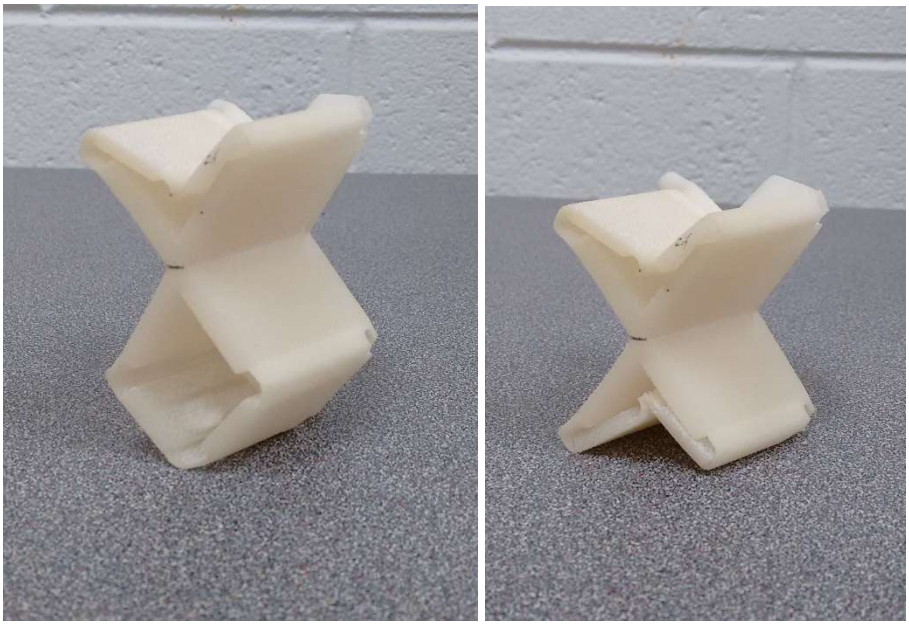

Figure 6.2 Four stable configurations of the dual cell chain

The four stable configurations can be seen in the above figure 6.2 namely, the '++' configuration (both cells in '+' state), the intermediate '+-' and '-+' configurations (the two cells in opposite state) and the '--' configuration (both cells in '-' state). This shows the ability of the Miura chain to exist in multiple stable configurations. However, further analysis of the stiffness of the Miura chain proved that the number of stable configurations of the chain with unique stiffness is less than the total number of stable configurations. For instance, in the above case of the dual cell Miura chain (m = 2), there are only three stable configurations with unique magnitudes of stiffness. This happens because the unit cells in a chain are assumed identical, thus intermediate configurations from Figure 6.2 (that is '+-

’ and ‘-+’ states) have the same magnitude of stiffness. In a more general statement, for a Miura chain with ‘m’ cells, there exist a total of 2^m stable configurations, among these stable states, there exist (m + 1) unique stiffness magnitudes. Another result from the analysis showed that the stiffness of the chain is the lowest when all the cells are in the ‘+’ configuration and the most when all the cells are in the ‘-’ configuration. In between, the stiffness magnitude of the chain increases as the number of cells in the ‘-’ configuration increases. This can be shown in the form of bar graphs which plot the stiffness magnitudes of a Miura chain with ‘m’ cells (Figure 6.3 to 6.6). The stiffness magnitudes represented by the bars are normalized $\left(K / \left[k_i / a_i\right]\right)$. The Matlab scripts used to generate the stiffness bar graphs shown below are given in Appendix C.

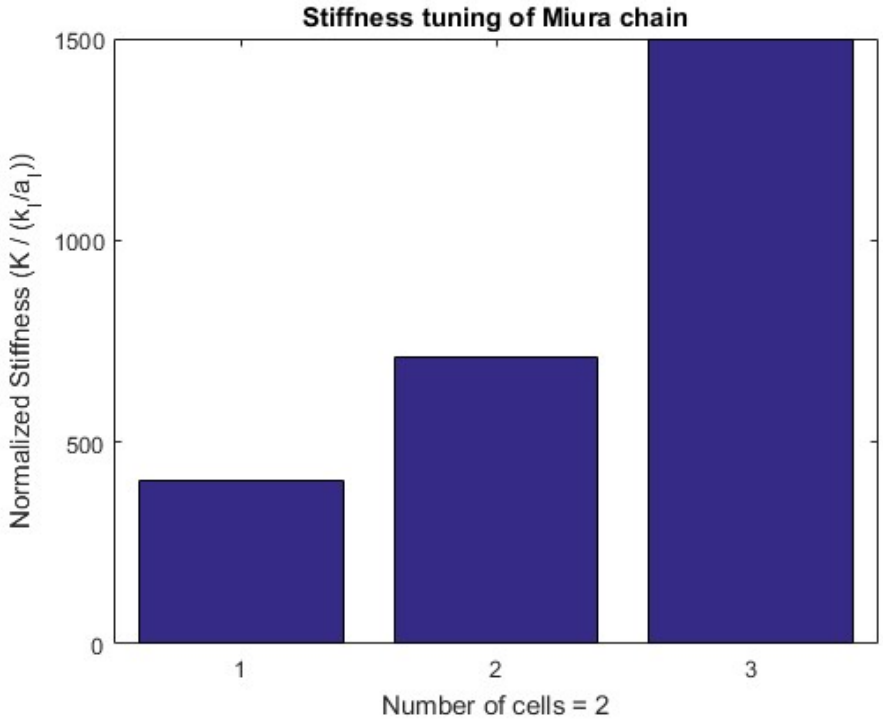

Figure 6.3 Stiffness magnitudes of Miura chain with 2 cells

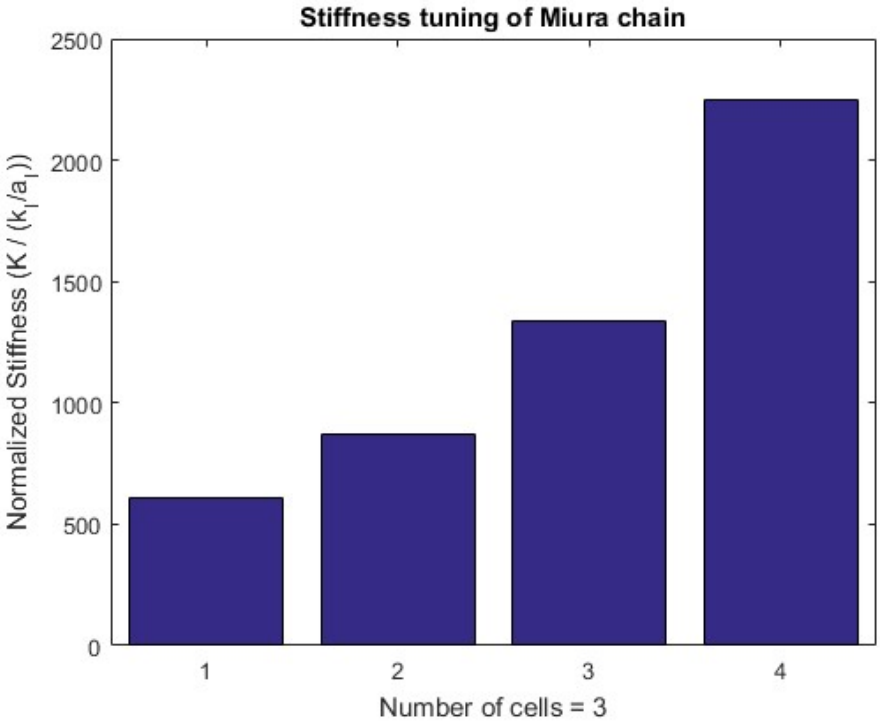

Figure 6.4 Stiffness magnitudes of Miura chain with 3 cells

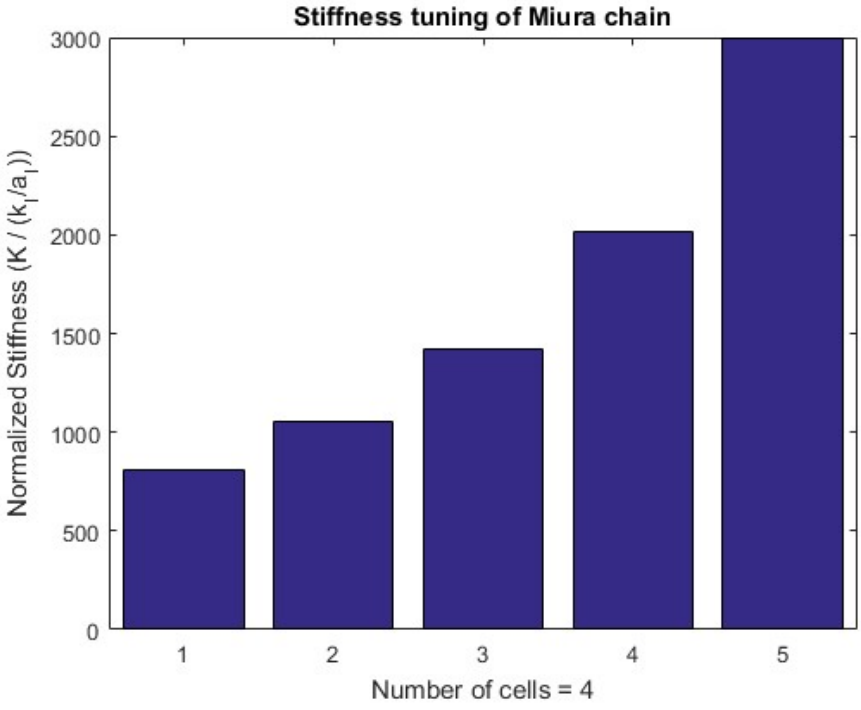

Figure 6.5 Stiffness magnitudes of Miura chain with 4 cells

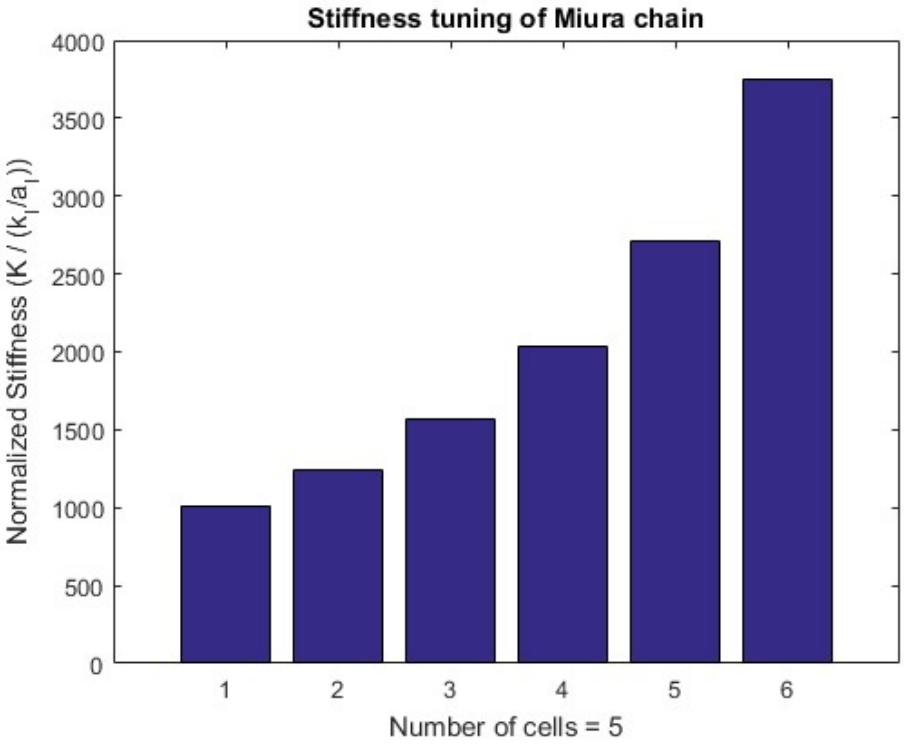

Figure 6.6 Stiffness magnitudes of Miura chain with 5 cells

In the case shown in figure 6.4, there are 3 cells in the chain. The stiffness of the first configuration ('+++') is the least, followed by two intermediate configurations ('++-' or '+-+' or '-++') and ('+--' or '-+-' or '--+'), while the last configuration ('---') has the highest magnitude of stiffness. As can be seen from Figures 6.3 through 6.6, there are (m + 1) possible configurations of a Miura chain with unique stiffness magnitudes. The stiffness bars in the figures 6.3 to 6.6 are arranged in an order such that in the configuration of the chain in the stiffness represented by the first bar, there are 0 cells in '-' configuration in the chain, for that in the second bar, there is 1 cell in the '-' configuration, for the i^{th} bar, there are i-1 cells in the '-' configuration, and in the $(m + 1)^{th}$ bar, 'm' or all the cells are in

the ‘-’ configuration. The stiffness magnitude bar graphs of Miura chains with a large number of cells (m = 7, 9, 11, 15) are shown in Appendix D.

The stiffness distribution as seen from the figures 6.3 through 6.6 show that the stiffness magnitudes increase in even steps as more cells in the chain are switched to the nested in ‘-’ configuration. Thus, if the switching of the individual cells can be continuously controlled by dynamic pressurization of the cells [21], it is possible to uniformly increase the stiffness of the chain from its lowest to highest magnitude or vice versa. When the cells in such a Miura chain are switched between different stable configurations, the chain possess programmable stiffness. Or in other words, the Miura chain can be switched to a particular configuration to achieve a desired stiffness.

CHAPTER SEVEN

CONCLUSIONS AND FUTURE WORK

This chapter sums up the research conclusions of the study presented in this thesis. Potential applications that can be targeted based on the conclusions from this study are also identified. In the end, some interesting future research topics are recommended.

7.1 Conclusions

The objective of this study is to examine how to harness the unique three-dimensional multi-stability of a Miura-Ori structure to achieve variable stiffness. In particular, this study focuses on the design of an elementary unit Miura cell to explore the physical principles. This unit cell is elastically bistable because of the non-linear relationships between the rigid-folding deformation and the crease material bending. Because of the unique nature of bistability, the stiffness of the unit cell is variable between its two stable configurations. Since the effective elastic modulus of the unit cell can be calculated from its stiffness, the study also explores the variable elastic modulus of the cell.

A parametric design analysis is carried out to highlight how the variable stiffness and elastic modulus can be programmed by prescribing certain key geometric parameters. The analysis shows that varying the crease length ratios and the sector angle can significantly affect the variable stiffness performance. The design space explored in this parametric analysis also provides a framework to pick a design for the bistable unit cell based on targeted performance viz. variable stiffness and elastic modulus.

A design is selected for the unit Miura cell from which a CAD model is generated which is used to 3D print a prototype. Two versions of this design prototype are 3D-printed, they differ in material selection and the type of 3D-printing process used. The unit cell prototype printed using an elasto-plastic material on a SLS printer is selected for experimentations. Compressive testing of this prototype provides the test data in the form of force-displacement curves and the stiffness is calculated as the slope of these curves. The stiffness ratio across the two stable configurations of the unit cell (K_- / K_+) obtained from the experimental results show a good match to those expected from the theoretical calculations. There are however, certain assumptions that are made to compare these results since the absolute elastic modulus of the 3D printed material is unknown. Despite this, the results are not affected since the objective of this work is to study the stiffness ratio and this does not change with the material properties.

After a comprehensive study of the unit cell along with experimental validations, the results from this study are extended to a Miura chain which is made up of multiple identical unit cells. The analysis of this Miura chain provides certain interesting insights into how the chain can display programmable stiffness by snapping the individual cells in it from one stable configuration to another. It is also seen that there exist multiple stable configurations for the chain, but there are certain equivalent configurations where the stiffness of the chain remains the same. This analysis of the Miura chain lays the groundwork for extending the study to a large-scale, multi-cellular Miura-Ori meta-structure with experimental validations.

7.2 Broader Impact

The unique nature of the multi-stability and the design framework from this work can be used to harness other unique mechanical properties which such meta-structures might be capable of. This study also provides a parametric analysis of the unit cell of a Miura-ori meta-structure which can be used as a design tool for further studies of such structures. The experimental validation of this design study ensures that this multi-stable Miura design can have potential applications in shape morphing structures and soft robotics.

7.3 Future Scope

7.3.1 Improving the existing analytical model

One of the gaps between the analytical study presented in this work and the actual fabrication of a physical prototype is that the analytical model does not fully consider several issues with manufacturing and material behaviors. For example, since origami is conventionally practiced with paper, the study does not take into account the thickness of engineering materials to be used for fabricating physical models. An improved analytical model can be built to take into account these considerations. The development of such an improved analytical model can also lead to a better exploration of the design space provided in this study.

7.3.2 Optimization of design space

This study provides a parametric analysis of the design space to relate the design parameters to the variable stiffness and elastic modulus. This parametric study can be further extended to include an optimization of the design space which would make it possible to select a design of the unit Miura cell based on targeted maximum or minimum performance required. Certain manufacturing constraints can also be introduced to narrow down the selection range of the input parameters. This optimization study can lead to the development of an inverse design methodology where a design is generated to meet the requirements.

7.3.3 Materials selection study

The fabrication of the unit cell prototypes showed that the materials available for 3D-printing were limited and the material parameters defined in the study were dictated by the properties of these available materials. Since some of these materials are relatively new to the 3D-printing industry, the manufacturers refrain from advertising all of the material properties publicly. A comprehensive materials selection study can be carried out first to identify all suitable materials, and then a closer analysis of these materials would result in selecting a material which would meet all design requirements. This study can also be potentially extended to also include other means of fabricating prototypes and identifying suitable materials for these fabrication techniques.

7.3.4 Stiffness distribution of the Miura chain

The analysis of the Miura chain shows that it is possible to have a 'tunable' stiffness by switching between different stable configurations of each unit cell in the chain. The stiffness of the chain increases as the number of cells in the '-' configuration increase. The distribution of this stiffness can be studied further to see how it can be related to the origami design and the internal folding configuration of the Miura chain. This would make it possible to identify a unit cell design and a specific folding configuration of the chain to achieve a targeted stiffness magnitude.

REFERENCES

[1] McArthur, M., Lang, R. J., Folding Paper: The Infinite Possibilities of Origami, 1sted., Tuttle Publishing, Rutland, VT, USA (2013).

[2] Greenberg, H. C., et al. "Identifying links between origami and compliant mechanisms." Mechanical Sciences 2.2 (2011): 217-225.

[3] Bowen, Landen A., et al. "A classification of action origami as systems of spherical mechanisms." Journal of Mechanical Design 135.11 (2013): 111008.

[4] Edmondson, Bryce J., et al. "Oriceps: Origami-Inspired Forceps." ASME 2013 Conference on Smart Materials, Adaptive Structures and Intelligent Systems. American Society of Mechanical Engineers, 2013.

[5] Shyu, Terry C., et al. "A kirigami approach to engineering elasticity in nanocomposites through patterned defects." Nature materials 14.8 (2015): 785-789.

[6] Saito, Kazuya, Fabio Agnese, and Fabrizio Scarpa. "A cellular kirigami morphing wingbox concept." Journal of intelligent material systems and structures 22.9 (2011): 935-944.

[7] Jianguo, Cai, Deng Xiaowei, and Feng Jian. "Morphology analysis of a foldable kirigami structure based on Miura origami." Smart Materials and Structures 23.9 (2014): 094011.

[8] Lebée, Arthur. "From folds to structures, a review." International Journal of Space Structures 30.2 (2015): 55-74.

[9] Peraza-Hernandez, Edwin A., et al. "Origami-inspired active structures: a synthesis and review." Smart Materials and Structures 23.9 (2014): 094001.

[10] Nishiyama, Yutaka. "Miura folding: Applying origami to space exploration." International Journal of Pure and Applied Mathematics 79.2 (2012): 269-279.

[11] Miura, Koryo, Hiroshi Furuya, and Kenichi Suzuki. "Variable geometry truss and its application to deployable truss and space crane arm." Acta Astronautica 12.7-8 (1985): 599-607.

[12] Miura, Koryo. "Method of packaging and deployment of large membranes in space." title The Institute of Space and Astronautical Science report 618 (1985): 1.

[13] Kuder, Izabela K., et al. "Variable stiffness material and structural concepts for morphing applications." Progress in Aerospace Sciences 63 (2013): 33-55.

[14] Schenk, Mark, and Simon D. Guest. "Geometry of Miura-folded metamaterials." Proceedings of the National Academy of Sciences 110.9 (2013): 3276-3281.

[15] Fang, Hongbin, Suyi Li, and K. W. Wang. "Self-locking degree-4 vertex origami structures." Proc. R. Soc. A. Vol. 472. No. 2195. The Royal Society, 2016.

[16] Turner, Nicholas, Bill Goodwine, and Mihir Sen. "A review of origami applications in mechanical engineering." Proceedings of the Institution of Mechanical Engineers, Part C: Journal of Mechanical Engineering Science 230.14 (2016): 2345-2362.

[17] Waitukaitis, Scott, et al. "Origami multistability: From single vertices to metasheets." Physical review letters 114.5 (2015): 055503.

[18] Silverberg, Jesse L., et al. "Origami structures with a critical transition to bistability arising from hidden degrees of freedom." Nature materials 14.4 (2015): 389-393.

[19] Hanna, Brandon H., et al. "Waterbomb base: a symmetric single-vertex bistable origami mechanism." Smart Materials and Structures 23.9 (2014): 094009.

[20] Jianguo, Cai, et al. "Bistable behavior of the cylindrical origami structure with Kresling pattern." Journal of Mechanical Design 137.6 (2015): 061406.

[21] Li, Suyi, and K. W. Wang. "Fluidic origami with embedded pressure dependent multi-stability: a plant inspired innovation." Journal of The Royal Society Interface 12.111 (2015): 20150639.

[22] Lipson, Hod, and Melba Kurman. Fabricated: The new world of 3D printing. John Wiley & Sons, 2013.

[23] Muth, Joseph T., et al. "Embedded 3D printing of strain sensors within highly stretchable elastomers." Advanced Materials 26.36 (2014): 6307-6312.

APPENDICES

APPENDIX A: ALTERNATE DESIGN PLOTS

The design plots show an alternate design when $\theta° = -55°$. It can be noted that the bistable area in the space is considerably reduced.

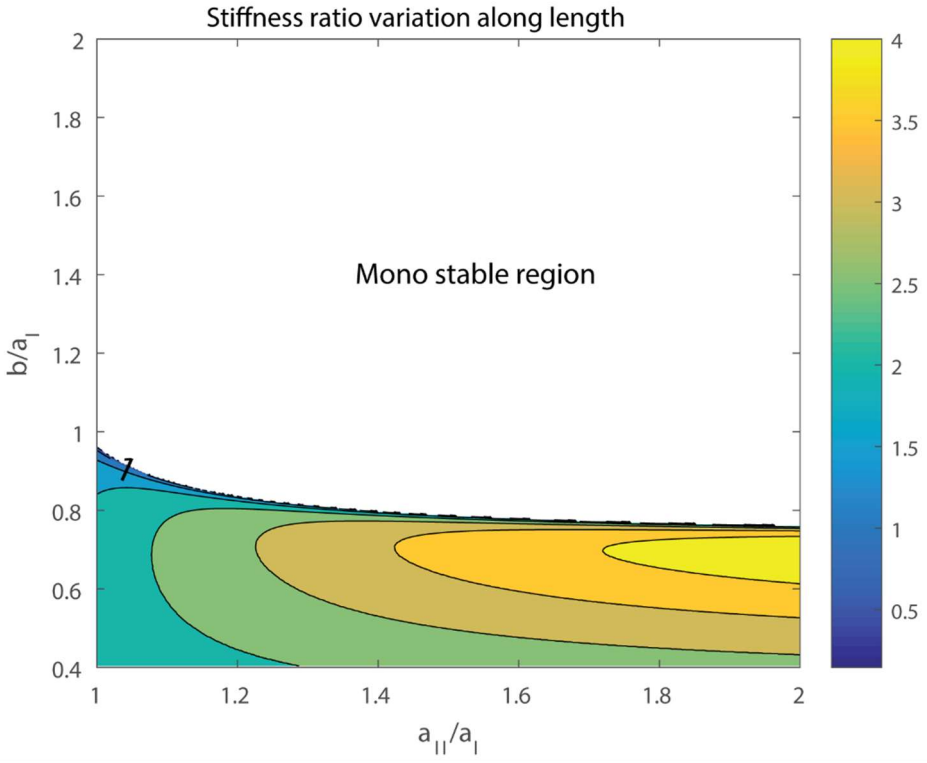

Figure A-1 Variation of b / a_I and a_{II} / a_I for stiffness ratio along length for $\theta° = -55°$

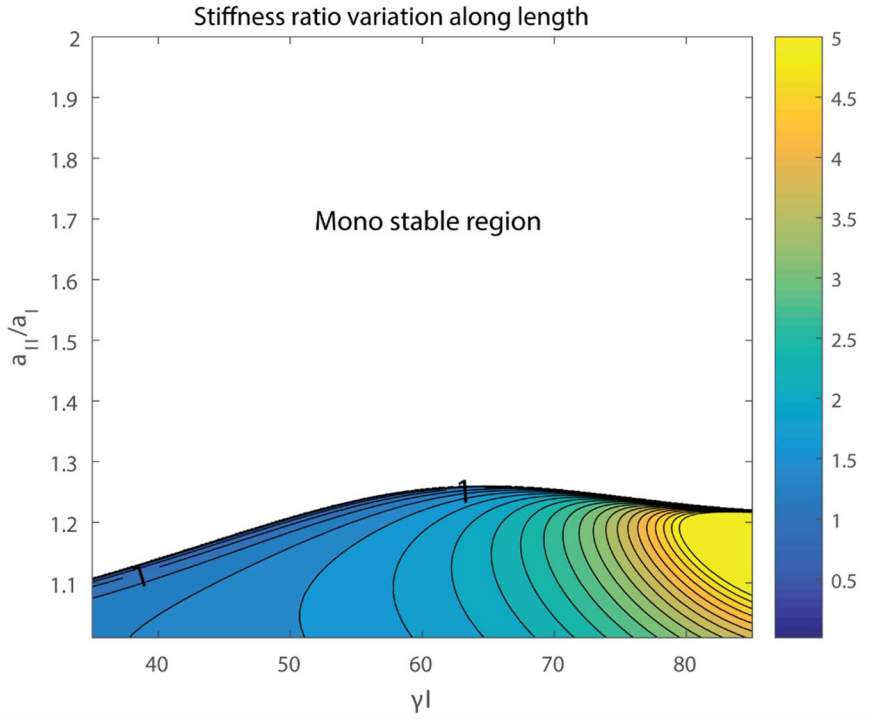

Figure A-2 Variation of a_{II} / a_I and γ_I for stiffness ratio along length for θ° = -55°

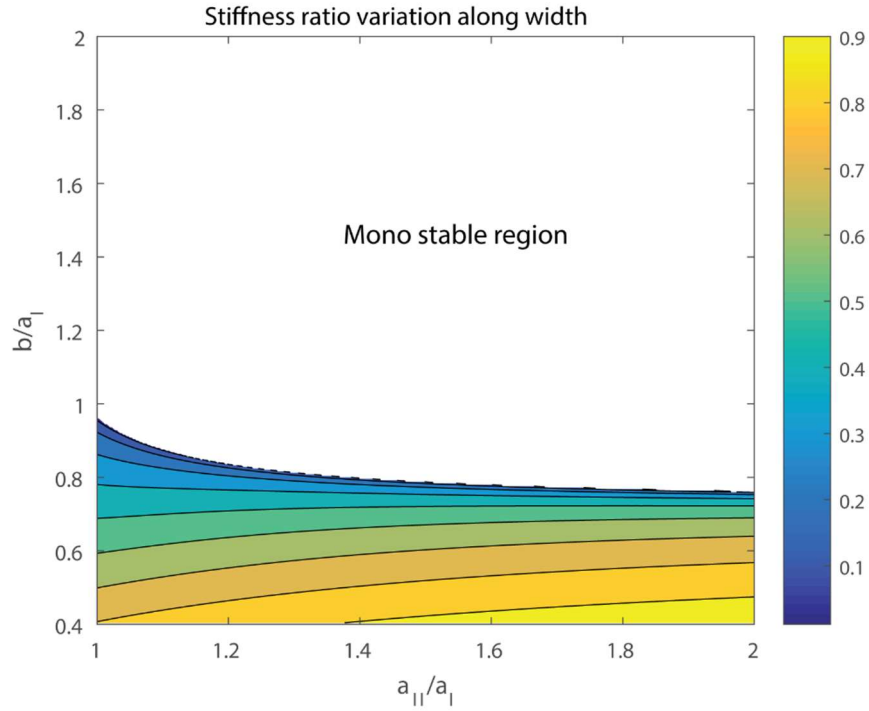

Figure A-3 Variation of b / a_I and a_{II} / a_I for stiffness ratio along width for θ° = -55°

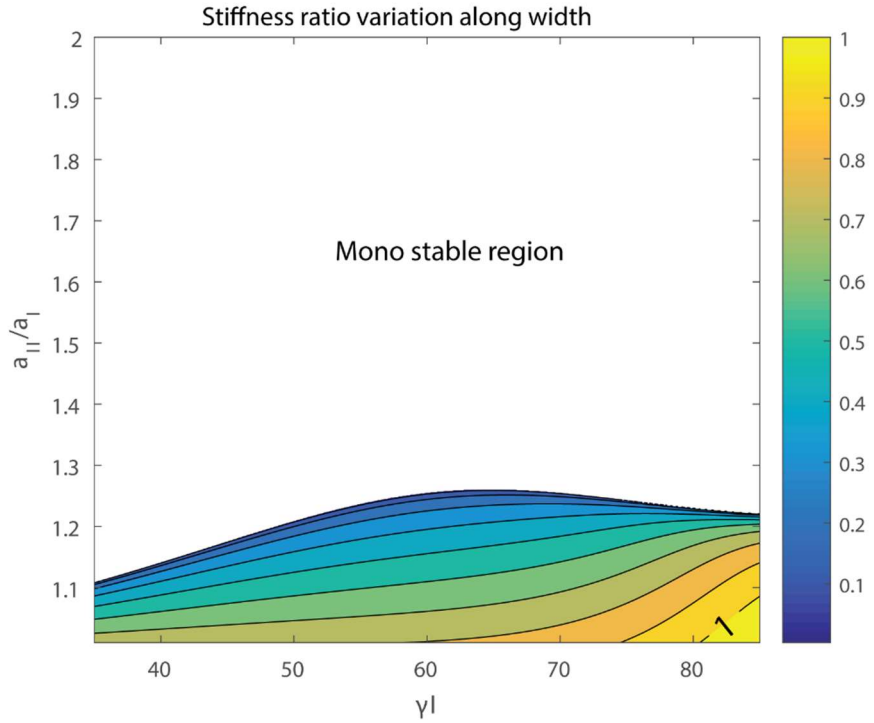

Figure A-4 Variation of a_{II} / a_I and γ_I for stiffness ratio along width for $\theta°$ = -55°

APPENDIX B: MATLAB SCRIPT FOR VARIABLE STIFFNESS AND ELASTIC MODULUS CALCULATIONS

```
%% Calculations for variable stiffness and elastic modulus
clear
clc
close all

aI = 25*(10^-3);
aII = 27.5*(10^-3);
b = 35*(10^-3);                 %defining
                                %geometric
gammaI = 75*(pi/180);           %parameters
gammaII = acos(cos(gammaI)*aI/aII);

kI = 5;                         %defining
kc = kI;                        %material
kII = 10*kI;                    %parameters

K1 = 2*kI*b;
K2 = 2*kI*aI;                   %torsional
K3 = 2*kII*b;                   %spring stiffness
K4 = 2*kII*aII;                 %constants
K5 = 4*kc*b;


h = 0.01;

thetaI = [-90:h:90]*(pi/180);   %range of
thetaI_plot = -90:h:90;         %folding angle

%defining stress free folding & dihedral angles
thetaIst = -60*(pi/180);

thetaIIst = acos((cos(thetaIst)*tan(gammaI))/tan(gammaII));

phiIst = pi - 2*thetaIst;
phiIIst = 2*pi - 2*asin(cos(thetaIst)/(sqrt(1-
((sin(thetaIst)*sin(gammaI))^2))));
phiIIIst = pi - 2*thetaIIst;
phiIVst = 2*asin((sin(gammaI)/sin(gammaII))*sin(phiIIst/2));
phiVst = thetaIIst - thetaIst;


%loop for calculating spring potential energy
for i=1:length(thetaI)

    thetaII(i) = acos((cos(thetaI(i))*tan(gammaI))/tan(gammaII));
    thetaIIst(i) = acos((cos(thetaIst)*tan(gammaI))/tan(gammaII));
```

```
    phiI(i) = pi - 2*thetaI(i);
    phiII(i) = 2*asin(cos(thetaI(i))/(sqrt(1-
((sin(thetaI(i))*sin(gammaI))^2))));
    phiIII(i) = pi - 2*thetaII(i);
    phiIV(i) = 2*asin((sin(gammaI)/sin(gammaII))*sin(phiII(i)/2));
    phiV(i) = thetaII(i) - thetaI(i);

    L(i) =
(2*b*cos(thetaI(i))*tan(gammaI))/sqrt(1+(cos(thetaI(i))*tan(gammaI))^2)
;
    W(i) = 2*aI*sqrt(1-(sin(thetaI(i))*sin(gammaI))^2);
    H(i) = aII*sin(thetaII(i))*sin(gammaII) -
aI*sin(thetaI(i))*sin(gammaI);

end

phiII(1:length(phiII)/2) = 2*pi - phiII(1:length(phiII)/2);

for i=1:length(thetaI)
    Ek(i) = (1/2)*(K1*(phiI(i) - phiIst)^2+K2*(phiII(i) -
phiIIst)^2+K3*(phiIII(i) - phiIIIst)^2+K4*(phiIV(i) -
phiIVst)^2+K5*(phiV(i) - phiVst)^2);
end


%% Height
HCentral = H(2:end-1);
H2Central = HCentral(2:end-1);

%force using numerical differentiation
Fh = (Ek(3:end)-Ek(1:end-2))./((H(3:end)-H(1:end-2)));
%stiffness using numerical differentiation
Kh = (Fh(3:end)-Fh(1:end-2))./((HCentral(3:end)-HCentral(1:end-2)));

%finding zero crossover points
h_indices = find([0 diff(sign(Fh))]~=0);

% defining normalized terms
Ek_norm = Ek/K2;
H_norm = H/aI;
HCentral_norm = HCentral/aI;
H2Central_norm = H2Central/aI;
Fh_norm = Fh/kI;

figure % Energy Curve
plot(H_norm,Ek_norm,H_norm(h_indices),Ek_norm(h_indices),'ro')
xlabel('Normalized Height (H/a_1)'); ylabel('Normalized Energy
(E/K_2)')

figure  % Force Displacement Curve with crossover points
```

```
plot(HCentral_norm,Fh_norm,HCentral_norm(h_indices),Fh_norm(h_indices),
'rx')
xlabel('Normalized Height (H/a_1)'); ylabel('Normalized Force (F/k_I)')

Kh_ratio = Kh(h_indices([3])) / Kh(l_indices([1]));


%% Length
LCentral = L(2:end-1);
L2Central = LCentral(2:end-1);

%force using numerical differentiation
Fl = (Ek(3:end)-Ek(1:end-2))./((L(3:end)-L(1:end-2)));
%stiffness using numerical differentiation
Kl = (Fl(3:end)-Fl(1:end-2))./((LCentral(3:end)-LCentral(1:end-2)));

%finding zero crossover points
l_indices = find([0 diff(sign(Fl))]~=0);
%eliminating unwanted index
l_ind = [2];
l_indices(l_ind) = [];

%defining normalized terms
Ek_norm = Ek/K2;
L_norm = L/aI;
LCentral_norm = LCentral/aI;
L2Central_norm = L2Central/aI;
Fl_norm = Fl/kI;

figure % Energy Curve
plot(L_norm,Ek_norm,L_norm(l_indices([1 2 3])),Ek_norm(l_indices([1 2
3])),'ro')
xlabel('Normalized Length (L/a_1)'); ylabel('Normalized Energy
(E/K_2)')

figure  % Force Displacement Curve with crossover points
plot(LCentral_norm,Fl_norm,LCentral_norm(l_indices),Fl_norm(l_indices),
'rx')
xlabel('Normalized Length (L/a_1)')
ylabel('Normalized Force (F/k_I)')

Kl_ratio = Kl(l_indices([3])) / Kl(l_indices([1]))


%calculating elastic modulus ratio
A1_l_index3 = (1/2)*(aI^2)*sin(phiI(l_indices([3])));
A2_l_index3 = (1/2)*(aII^2)*sin(phiIII(l_indices([3])));
E_mod_l_index3 =
(Kl(l_indices([3]))*(L(l_indices([3]))))/(A1_l_index3+A2_l_index3);

A1_l_index1 = (1/2)*(aI^2)*sin(phiI(l_indices([1])));
```

```
A2_l_index1 = (1/2)*(aII^2)*sin(phiIII(l_indices([1])));

E_mod_l_index1 =
(Kl(l_indices([1]))*(L(l_indices([1]))))/(A1_l_index1+A2_l_index1);

E_mod_l_ratio = E_mod_l_index3 / E_mod_l_index1;


%% Width

WCentral = W(2:end-1);
W2Central = WCentral(2:end-1);

%force using numerical differentiation
Fw = (Ek(3:end)-Ek(1:end-2))./((W(3:end)-W(1:end-2)));
%stiffness using numerical differentiation
Kw = (Fw(3:end)-Fw(1:end-2))./((WCentral(3:end)-WCentral(1:end-2)));

%finding zero crossover points
w_indices = find([0 diff(sign(Fw))]~=0);
%eliminating unwanted index
w_ind = [2];
w_indices(w_ind) = [];

%defining normaized terms
Ek_norm = Ek/K2;
W_norm = W/aI;
WCentral_norm = WCentral/aI;
W2Central_norm = W2Central/aI;
Fw_norm = Fw/kI;

figure % Energy Curve
plot(W_norm,Ek_norm,W_norm(w_indices),Ek_norm(w_indices),'ro')
xlabel('Normalized Width (W/a_1)'); ylabel('Normalized Energy (E/K_2)')


figure  % Force Displacement Curve with crossover points
plot(WCentral_norm,Fw_norm,WCentral_norm(w_indices),Fw_norm(w_indices),
'rx')
xlabel('Normalized Width (W/a_1)')
ylabel('Normalized Force (F/k_I)')


Kw_ratio = Kw(w_indices([3])) / Kw(w_indices([1]));


%calculating elastic modulus
A_w_index3 = H(w_indices([3]))*L(w_indices([3]));
E_mod_w_index3 = (Kw(w_indices([3]))*(W(w_indices([3]))))/(A_w_index3);
```

```
A_w_index1 = L(w_indices([1]))*(aII*cos(phiIII(w_indices([1]))/2) -
aI*cos(phiI(w_indices([1]))/2));
E_mod_w_index1 = (Kw(w_indices([1]))*(W(w_indices([1])))))/(A_w_index1);

E_mod_w_ratio = E_mod_w_index3 / E_mod_w_index1;
```

APPENDIX C: MATLAB SCRIPT FOR CALCULATING PROGRAMMABLE STIFFNESS FOR MIURA CHAIN WITH SAMPLE OUTPUTS

```
% Identifying number of unique stiffness configurations in a Miura
column with 'm' cells

clear
clc
close all

prompt = 'number of cells in column? ';
m = input(prompt);                              % number of cells in a
                                                    column
tpc = 2^m;                                      % total number of possible
                                                    configurations
no_m = 1:m+1;                                   % number of configurations
                                        with unique stiffness magnitudes

%% Design parameters

aI = 25*(10^-3);                                % facet lengths
aII = 27.5*(10^-3);
b = 35*(10^-3);

gammaI = 75*(pi/180);                           % angle between adjacent
facets
gammaII = acos(cos(gammaI)*aI/aII);

kI = 5;                                         % crease stiffnesses per
                                                    unit length (*)
kc = kI;
kII = 10*kI;



K1 = 2*kI*b;
K2 = 2*kI*aI;
K3 = 2*kII*b;
K4 = 2*kII*aII;
K5 = 4*kc*b;

%% Energy (Case 1)

h1 = 0.01;

thetaI_case1 = [-90:h1:90]*(pi/180);
thetaI_case1_plot = [-90:h1:90];

thetaIst_case1 = -60*(pi/180);
```

```
thetaIIst_case1 = acos((cos(thetaIst_case1)*tan(gammaI))/tan(gammaII));

phiIst_case1 = pi - 2*thetaIst_case1;
phiIIst_case1 = 2*pi - 2*asin(cos(thetaIst_case1)/(sqrt(1-
((sin(thetaIst_case1)*sin(gammaI))^2))));
phiIIIst_case1 = pi - 2*thetaIIst_case1;
phiIVst_case1 =
2*asin((sin(gammaI)/sin(gammaII))*sin(phiIIst_case1/2));
phiVst_case1 = thetaIIst_case1 - thetaIst_case1;

for i=1:length(thetaI_case1)

    thetaII_case1(i) =
acos((cos(thetaI_case1(i))*tan(gammaI))/tan(gammaII));
    thetaIIst_case1(i) =
acos((cos(thetaIst_case1)*tan(gammaI))/tan(gammaII));

    phiI_case1(i) = pi - 2*thetaI_case1(i);
    phiII_case1(i) = 2*asin(cos(thetaI_case1(i))/(sqrt(1-
((sin(thetaI_case1(i))*sin(gammaI))^2))));
    phiIII_case1(i) = pi - 2*thetaII_case1(i);
    phiIV_case1(i) =
2*asin((sin(gammaI)/sin(gammaII))*sin(phiII_case1(i)/2));
    phiV_case1(i) = thetaII_case1(i) - thetaI_case1(i);

    L_case1(i) =
(2*b*cos(thetaI_case1(i))*tan(gammaI))/sqrt(1+(cos(thetaI_case1(i))*tan
(gammaI))^2);
    W_case1(i) = 2*aI*sqrt(1-(sin(thetaI_case1(i))*sin(gammaI))^2);
    H_case1(i) = aII*sin(thetaII_case1(i))*sin(gammaII) -
aI*sin(thetaI_case1(i))*sin(gammaI);

end

phiII_case1(1:length(phiII_case1)/2) = 2*pi -
phiII_case1(1:length(phiII_case1)/2);

for i=1:length(thetaI_case1)
    Ek_case1(i) = (1/2)*(K1*(phiI_case1(i) -
phiIst_case1)^2+K2*(phiII_case1(i) -
phiIIst_case1)^2+K3*(phiIII_case1(i) -
phiIIIst_case1)^2+K4*(phiIV_case1(i) -
phiIVst_case1)^2+K5*(phiV_case1(i) - phiVst_case1)^2);
end


%% Energy (Case 2)
Ek_case2 = fliplr(Ek_case1);


%% Calculating all stiffnesses
```

```
M = combinator(2,m,'p','r');

LCentral = L_case2(2:end-1);
L2Central = LCentral(2:end-1);


for i=1:length(Ek_case1)
    temp = M;
    temp(temp==1) = Ek_case1(i);
    temp(temp==2) = Ek_case2(i);

    for j = 1:tpc;

        all_Ek(j,i) = sum(temp(j,:));

    end
end

for k= 1:tpc

    all_Fl = (all_Ek(k,(3:end)) - all_Ek(k,(1:end-
2)))./((L_case2(3:end)-L_case2(1:end-2)));

    all_Kl = (all_Fl(3:end) - all_Fl(1:end-2))./((LCentral(3:end)-
LCentral(1:end-2)));

    l_indices = find([0 diff(sign(all_Fl))]~=0);
    l_ind = [3];
    l_indices(l_ind) = [];
    K_pull(k) = all_Kl(l_indices([1]));
    K_all(k) = round(K_pull(k),-1);


fprintf('Total possible configurations for %d cells is %d =
(2^m)\n',m,tpc);

K_usc = unique(K_all,'stable');
K_norm = K_usc/(kI/aI);

for j1 = 1:m+1
    K_ratios(j1) = K_usc(j1)/K_usc(1);
    K_disp(j1) = K_norm(j1)/K_norm(1);
end

fprintf('But, configurations with unique stiffness are %d = (m +
1)\n',length(K_usc));

figure
bar(no_m,K_norm)
```

```
xlabel(['Number of cells = ' num2str(m)])
ylabel('Normalized Stiffness (K / (k_I/a_I))');
title('Stiffness tuning of Miura chain')

fprintf('The stiffness ratios are:')

for p=1:m

    fprintf('\nK(%d)/K(1) = %4.2f\n',p+1,K_usc(p+1)/K_usc(1));

end
```

Sample outputs for *m*=4 and *m*=7

***m* = 4**

number of cells in column? 4

Total possible configurations for 4 cells is 16 = (2^m)

But, configurations with unique stiffness are 5 = (m + 1)

The stiffness ratios are:

K(2)/K(1) = 1.30

K(3)/K(1) = 1.75

K(4)/K(1) = 2.48

K(5)/K(1) = 3.69

***m* = 7**

number of cells in column? 7

Total possible configurations for 7 cells is 128 = (2^m)

But, configurations with unique stiffness are 8 = (m + 1)

The stiffness ratios are:

K(2)/K(1) = 1.15

K(3)/K(1) = 1.35

K(4)/K(1) = 1.60

K(5)/K(1) = 1.92

K(6)/K(1) = 2.35

K(7)/K(1) = 2.92

K(8)/K(1) = 3.69

APPENDIX D: ADDITIONAL PROGRAMMABLE STIFFNESS PLOTS FOR MIURA CHAINS

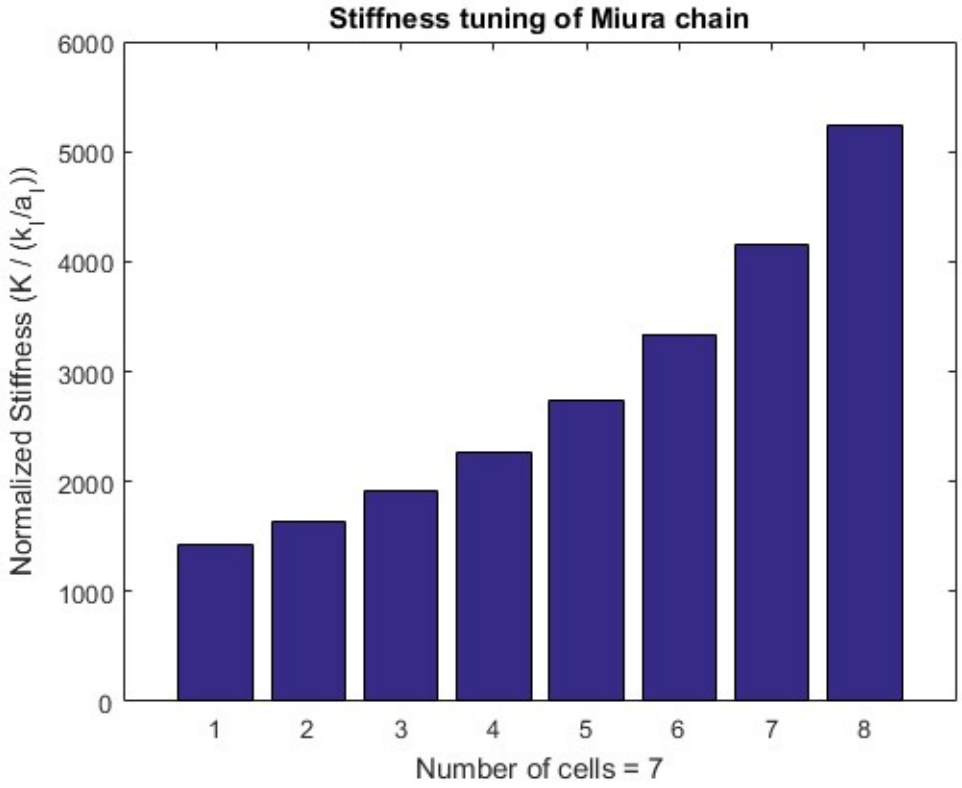

Figure D-1 Stiffness magnitudes of Miura chain with 7 cells

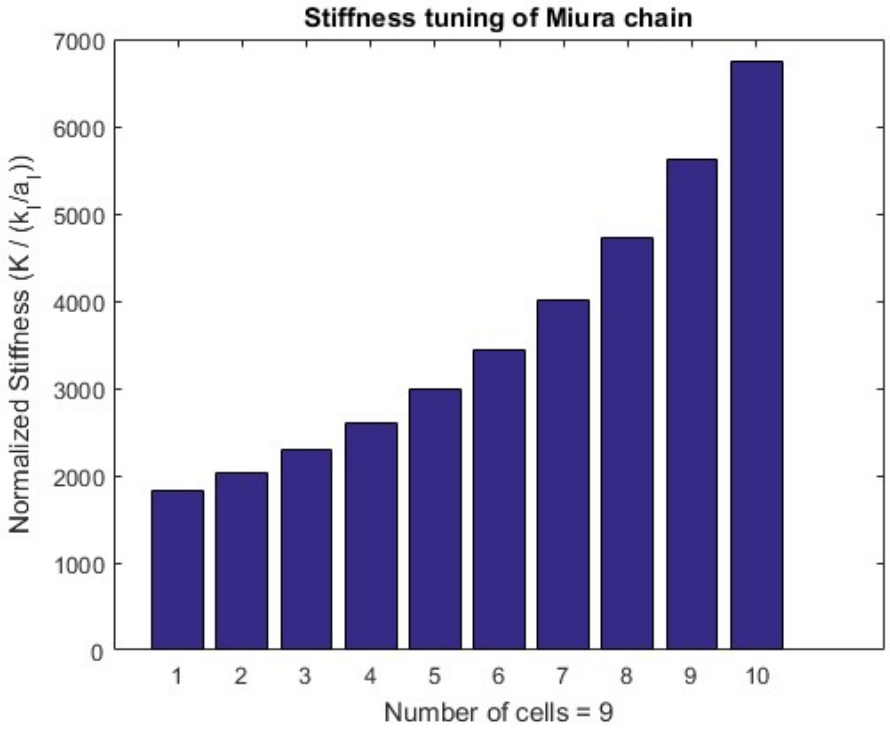

Figure D-2 Stiffness magnitudes of Miura chain with 9 cells

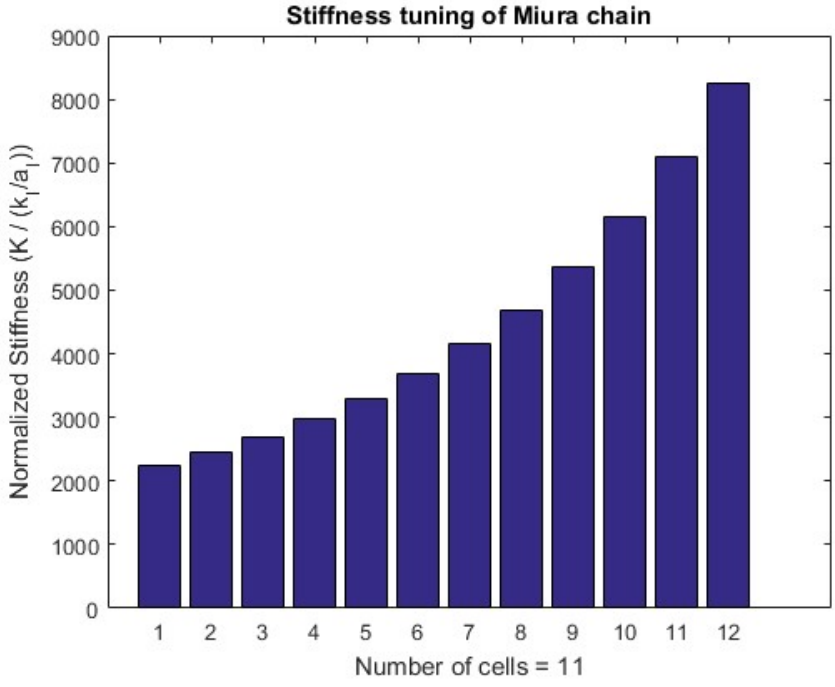

Figure D-3 Stiffness magnitudes of Miura chain with 11 cells

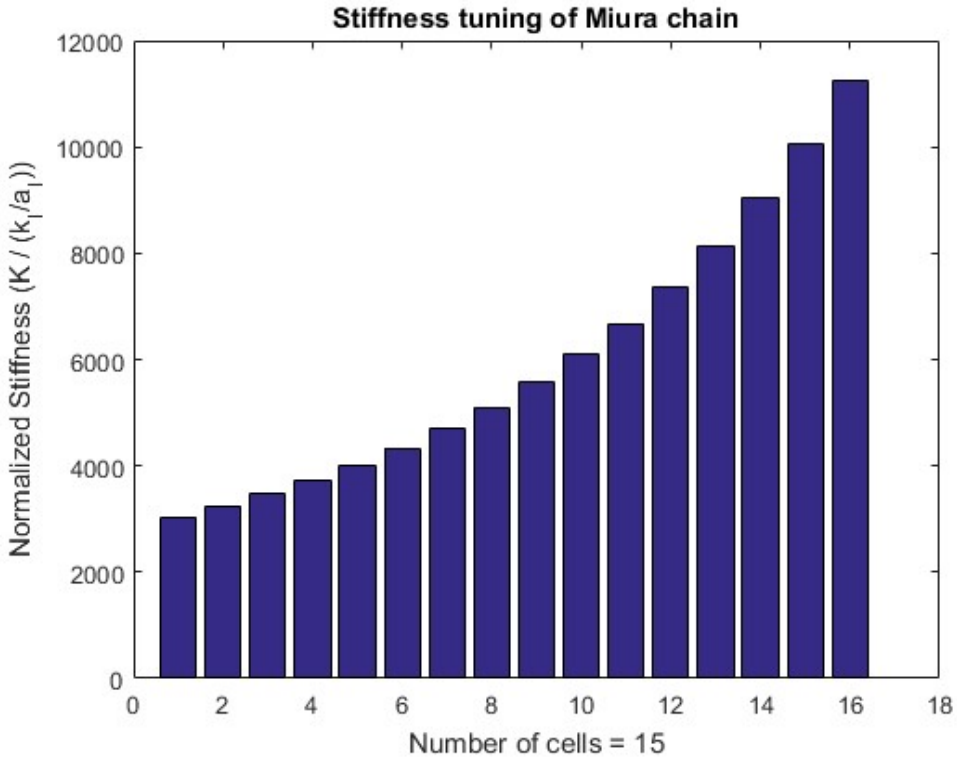

Figure D-4 Stiffness magnitudes of Miura chain with 15 cells